



HAL
open science

Experimental investigations on the dynamic behavior of a 2-DOF airfoil in the transitional Re number regime based on digital-image correlation measurements

Jens Nikolas Wood, Michael Breuer, Guillaume de Nayer

► To cite this version:

Jens Nikolas Wood, Michael Breuer, Guillaume de Nayer. Experimental investigations on the dynamic behavior of a 2-DOF airfoil in the transitional Re number regime based on digital-image correlation measurements. *Journal of Fluids and Structures*, 2020, 96, 10.1016/j.jfluidstructs.2020.103052 . hal-02650032

HAL Id: hal-02650032

<https://hal.science/hal-02650032>

Submitted on 29 May 2020

HAL is a multi-disciplinary open access archive for the deposit and dissemination of scientific research documents, whether they are published or not. The documents may come from teaching and research institutions in France or abroad, or from public or private research centers.

L'archive ouverte pluridisciplinaire **HAL**, est destinée au dépôt et à la diffusion de documents scientifiques de niveau recherche, publiés ou non, émanant des établissements d'enseignement et de recherche français ou étrangers, des laboratoires publics ou privés.



Distributed under a Creative Commons Attribution 4.0 International License



Experimental investigations on the dynamic behavior of a 2-DOF airfoil in the transitional Re number regime based on digital-image correlation measurements



J.N. Wood, M. Breuer*, G. De Nayer

Professur für Strömungsmechanik, Helmut-Schmidt-Universität Hamburg, D-22043 Hamburg, Germany

ARTICLE INFO

Article history:

Received 17 October 2019

Received in revised form 11 May 2020

Accepted 18 May 2020

Available online xxxx

Keywords:

Fluid–structure interaction

2-DOF aeroelastic oscillations

Limit-cycle oscillation

Airfoil flutter

Wind tunnel experiments

Digital-image correlation

ABSTRACT

The present paper investigates the fluid–structure interaction (FSI) of a wing with two degrees of freedom (DOF), i.e., pitch and heave, in the transitional Reynolds number regime. This 2-DOF setup marks a classic configuration in aeroelasticity to demonstrate flutter stability of wings. In the past, mainly analytic approaches have been developed to investigate this challenging problem under simplifying assumptions such as potential flow. Although the classical theory offers satisfying results for certain cases, modern numerical simulations based on fully coupled approaches, which are more generally applicable and powerful, are still rarely found. Thus, the aim of this paper is to provide appropriate experimental reference data for well-defined configurations under clear operating conditions. In a follow-up contribution these will be used to demonstrate the capability of modern simulation techniques to capture instantaneous physical phenomena such as flutter. The measurements in a wind tunnel are carried out based on digital-image correlation (DIC). The investigated setup consists of a straight wing using a symmetric NACA 0012 airfoil. For the experiments the model is mounted into a frame by means of bending and torsional springs imitating the elastic behavior of the wing. Three different configurations of the wing possessing a fixed elastic axis are considered. For this purpose, the center of gravity is shifted along the chord line of the airfoil influencing the flutter stability of the setup. Still air free-oscillation tests are used to determine characteristic properties of the unloaded system (e.g. mass moment of inertia and damping ratios) for one (pitch or heave) and two degrees (pitch and heave) of freedom. The investigations on the coupled 2-DOF system in the wind tunnel are performed in an overall chord Reynolds number range of $9.66 \times 10^3 \leq Re \leq 8.77 \times 10^4$. The effect of the fluid-load induced damping is studied for the three configurations. Furthermore, the cases of limit-cycle oscillation (LCO) as well as diverging flutter motion of the wing are characterized in detail. In addition to the DIC measurements, hot-film measurements of the wake flow for the rigid and the oscillating airfoil are presented in order to distinguish effects originating from the flow and the structure.

© 2020 The Authors. Published by Elsevier Ltd. This is an open access article under the CC BY license (<http://creativecommons.org/licenses/by/4.0/>).

1. Introduction

Modern computing capabilities allow the accurate simulation of complex coupled problems such as fluid–structure interaction (FSI). However, the numerical methods have to be validated in order to guarantee physically meaningful

* Corresponding author.

E-mail address: breuer@hsu-hh.de (M. Breuer).

results. The validation is often based on reference data taken from comparable experimental studies. For this purpose, all relevant parameters and boundary conditions of the observed physical system have to be accurately determined in the experiment and transferred to the numerics to ensure comparability. This complementary experimental–numerical approach has been successfully applied to several well-established benchmark cases for FSI (Breuer et al., 2012; De Nayer et al., 2014; De Nayer and Breuer, 2014; Gomes and Lienhart, 2010; Gomes et al., 2010; Gomes and Lienhart, 2013; Kalmbach and Breuer, 2013). These cases mainly focused on the oscillations and deformations of a flexible plate mounted to the lee-side of a rigid body. In these FSI benchmarks the elastic plate was excited by vortex shedding past the rigid body. Going a step further, fully three-dimensional FSI investigations of a flexible membranous hemisphere immersed in a turbulent boundary layer flow were carried out in a complementary experimental–numerical study (Apostolatos et al., 2019; De Nayer et al., 2018; Wood et al., 2018; Wood, 2019). The highly elastic thin structure was excited by the turbulent flow showing complex deformation patterns on the lee-side of the hemisphere. The dominant FSI mechanisms involved were associated with vortex-induced vibrations caused by the formation and shedding of large-scale vortices.

The present FSI case considers the flow around a rigid body represented by a symmetric airfoil with two degrees of freedom (2-DOF), i.e., vertical translation (“heave”) and rotation about the spanwise axis (“pitch”). This configuration is inspired by classical investigations on aeroelasticity used for the analysis of flutter stability often restricted to two-dimensional airfoils. Furthermore, the Reynolds number range investigated, i.e., $10^3 \leq Re \leq 10^5$ falls into the transitional regime. Previous studies showed that this velocity range exhibits aeroelastic effects that are different compared to high-Re investigations outlined in classic text books (Bisplinghoff and Ashley, 2013; Dowell, 2015; Fung, 2008; Wright and Cooper, 2008) relying on simplifying approaches such as inviscid and irrotational flow (potential theory). Several interesting physical phenomena are observed in the transitional regime: At the lower-Re border the flow around the airfoil has a damping or stiffening effect on sudden wing oscillations caused by outer disturbances. Increasing the free-stream velocity typically leads to limit-cycle oscillations (LCO) with small and steady amplitudes connected to the laminar separation at the trailing edge of the airfoil mainly visible in the pitch degree of freedom. Within a specific free-stream velocity range the small amplitudes can rise to large amplitude LCO when provoked by an external disturbance. These oscillations are significantly larger but still exhibit limited amplitudes. Exceeding this Re range leads to an exponential growth of the amplitudes denoted as “flutter”. This phenomenon exhibits one unique flutter frequency in which both degrees of freedom oscillate. The 2-DOF oscillation is characterized by a case specific phase-shift angle between pitch and heave. A brief literature review on recent investigations in modern experimental facilities and based on numerical simulations is given in the following.

Wind tunnel experiments on the dynamic behavior of an elastically mounted NACA 0012 airfoil in a transitional Re number range of $4.5 \times 10^4 \leq Re \leq 1.3 \times 10^5$ were extensively conducted by Poirel et al. (2006, 2008). Major focus was put on the investigation of the aeroelastic effect of self-sustained oscillations occurring in a specific velocity range. Since these types of oscillations were sparsely investigated before, the conducted experiments allowed a deeper insight into the underlying excitation mechanisms. Although the experimental apparatus included a wing with two degrees of freedom, the studies were restricted to the pure pitch motion by blocking the heave mechanism of the wind tunnel model. All relevant parameters such as spring stiffness and damping ratio of the experimental setup were determined in still air. The study focused on the frequency response of the airfoil considering different configurations with variable spring stiffness and changing positions of the elastic axis. High-frequency vortices in the wake were measured by hot-wire anemometry and attributed to the presence of von Kármán vortices. These wake effects had no direct influence on the airfoil dynamics, because no frequency dependency between both effects was found. As a conclusion it was speculated that the presence of laminar flow separation near the trailing edge as well as a fluctuating laminar separation bubble (LSB) at the leading edge were the major sources for the excitation mechanism within a limited Re-range.

Based on these initial studies first attempts were made by Métivier et al. (2008, 2009) and Poirel et al. (2011) to conduct two-dimensional numerical simulations of the identical problem in order to verify the conclusions made in the previous experimental work. Again the aeroelastic oscillations of a NACA 0012 airfoil with a single DOF, i.e., pure pitch, were examined using a RANS flow solver with the SST $k-\omega$ turbulence model and a low-Re correction on an adaptable mesh. The simulations targeted explicitly at low-frequency and low-amplitude oscillations of the airfoil in the range $5 \times 10^4 \leq Re \leq 1.5 \times 10^5$. Two major findings were reported: First, the assumed laminar separation of the boundary layer near the trailing edge was confirmed. Second, the pitch motion of the airfoil did not respond to effects occurring in the wake regime, i.e., vortex shedding.

Another experimental contribution by Poirel and Mendes (2012) used the same aforementioned experimental setup (NACA 0012 airfoil) but now with 2-DOF (pitch and heave) in the range $5.5 \times 10^4 \leq Re \leq 1.25 \times 10^5$. In this study the stiffness of the pitch spring was kept constant while two different bending stiffnesses for the heave motion were considered. Based on these conditions the main objective was to investigate two types of limit-cycle oscillations denoted as “small-amplitude oscillations” (SAO) and “large-amplitude oscillations” (LAO). The SAO type is associated with the separation of the laminar boundary layer at the trailing edge leading to moderate and limited oscillations naturally occurring within a certain Re number range also described in detail by Poirel and Mendes (2014). This type of excitation of the airfoil is also denoted as “laminar separation flutter”. On the other hand, the LAO type is characterized by larger amplitudes appearing after an initial disturbance of the airfoil. In this oscillatory state, pitch and heave frequencies collapse to a single frequency with a certain phase-shift angle between both DOF. However, the amplitudes are limited to a maximum value and oscillate within this range. This oscillation type is associated with negative damping entirely driven by mode coupling of the structure and sustained by the energy transferred from the flow to the elastic structure.

Further numerical studies using a two-dimensional URANS approach (Spalart–Allmaras and γ - Re_θ models) were presented by Lapointe and Dumas (2012) examining the self-sustained pitch-heave oscillations of a NACA 0012 airfoil in the range $5 \times 10^4 \leq Re \leq 1.39 \times 10^5$. This study focused on the LAO type including very large pitch angles up to 97° . An interesting finding is that the magnitude of the phase angle between pitch and heave motion increases at higher Reynolds numbers. Furthermore, a visualization of the flow structures using a series of images of the instantaneous velocity field were used to illustrate the massively separated flow around the airfoil during one complete excitation cycle. As a conclusion the 2-DOF pitch-heave system is found to be dominated by dynamic stall and leading-edge vortex shedding.

A similar numerical investigation was carried out by Veilleux and Dumas (2013) using either no (laminar), the SST $k-\omega$ or the Spalart–Allmaras turbulence model. The simulations comprising five Re numbers ranging between 5×10^4 and 1.2×10^5 were compared to experimental studies (Poirel and Mendes, 2012). Furthermore, two heave stiffnesses taken from the experiments (Poirel and Mendes, 2012) were applied as well as three different damping coefficients denoted as “no damping”, “baseline damping” and “strong damping”. The parameters were implemented in a two-dimensional fluid–structure simulations setup using the open-source code *OpenFOAM*. Self-sustained oscillations of a NACA 0012 airfoil with large amplitudes were observed related to flutter. Within the investigated Re-range the frequency response of the laminar simulations showed the best agreement with the experiments especially for the lower bending stiffness case. At higher bending stiffnesses all three numerical models predicted almost the same trend for the maximum pitch angle as well as for the associated flutter frequencies. Interestingly, the implemented damping coefficients showed more or less the same behavior in all three numerical models resulting in an almost identical frequency response at all Re.

A three-dimensional large-eddy simulation (LES) based on the experimental parameters of Poirel et al. (2008) was performed by Yuan et al. (2012, 2013) at $Re = 7.7 \times 10^4$. This study explored the 1-DOF pitch as well as the 2-DOF heave-pitch system. The 1-DOF case was found to match remarkably well with the experiments confirming the presence of limit-cycle oscillations of the SAO type. In the 2-DOF case minor discrepancies were observed in the predictions due to the neglected dry friction that appears in a non-linear manner in the experiment induced by the mechanism of the heave motion. The reported frequency response was connected to a single LCO frequency. A final conclusion was the relatively low influence of the heave motion, which contributed only with a very small amplitude of about 1% of the chord length. Although the major part of the 2-DOF LCO was pitch driven, a significant amount of the work done by the aerodynamic load was attributed to the presence of the heave motion.

Further experimental studies by Kim et al. (2013) investigated the lift and pressure-drag coefficients of an airfoil in a pure pitch setup at $Re = 4.8 \times 10^4$. The setup comprised a wing with surface pressure drilling used to measure the unsteady pressure at specific locations on the airfoil, while limit-cycle oscillations occurred. The data revealed different hysteresis cycles of the lift and pressure-drag coefficients rotating in clockwise and counter-clockwise directions depending on Re. The driving effect behind this hysteresis is a characteristic reattachment of the flow during the pitching motion of the airfoil.

In a second study Kim and Chang (2014) examined the aerodynamic characteristics of a pitching NACA 0012 airfoil focusing on the effects occurring at three Re numbers, 2.3×10^4 , 3.3×10^4 and 4.8×10^4 . Flow visualization of the near wake was accomplished by images of a smoke wire. Again, the unsteady pressure was measured with the aforementioned experimental procedure (Kim et al., 2013) in order to determine lift and pressure-drag coefficients which could be linked to the smoke-wire images. The elastic axis was located at a quarter of the chord length with a zero mean angle of attack. The amplitude of the oscillations was $\pm 6^\circ$. The images of the flow revealed primary and secondary trailing-edge vortices and mushroom structures depending on Re. Hysteresis cycles were found in the data of the pressure measurements. These cycles were characterized by the dynamic behavior of the lift and pressure-drag coefficients. The phase-shift angle between lift and drag was found to be inversely proportional to Re. Based on this observation it was concluded that the pitching of the airfoil is mainly driven by the separation of the laminar boundary layer from the surface of the airfoil.

A recent study by Boudreau et al. (2020) presented the capability of a fully-passive flapping foil (NACA 0015) as a source for renewable energy. Numerical simulations were conducted at $Re = 3.9 \times 10^6$ based on a two-dimensional URANS methodology. The paper outlines the influence of the structural parameters of the 2-DOF system (pitch and heave) on the efficiency to extract energy. A parametric study of the structural parameters was carried out in order to identify the optimum operation state of the flapping foil. In conclusion, a system with a large static moment, i.e., a certain distance between the elastic axis and the center of mass, is the most efficient configuration emphasizing the importance of this parameter.

The objective of the present paper is the characterization of the dynamic behavior of a NACA 0012 airfoil in a 2-DOF pitch-heave setup. For this purpose, an especially designed experimental setup is applied in order to measure the unsteady displacements of the airfoil in the range $9.66 \times 10^3 \leq Re \leq 8.77 \times 10^4$. The measurements are complemented by free-oscillation tests in still air from which important parameters such as the natural eigenfrequencies of both DOF, the mass moment of inertia, the total damping ratio of the translational and torsional motion and the bending stiffness of the translational (heave) spring are evaluated. Three configurations with a fixed elastic axis and a variable center of gravity are used to investigate the flutter stability of each setup. As a novel approach for the characterization of the airfoil dynamics a stereoscopic setup of high-speed cameras is used to record the oscillations. The time-dependent displacements in the vertical direction are measured by digital-image correlation (DIC). From these data the frequency response is determined by a fast Fourier transform. Additional hot-film measurements of the wake flow for the rigid and the elastically mounted

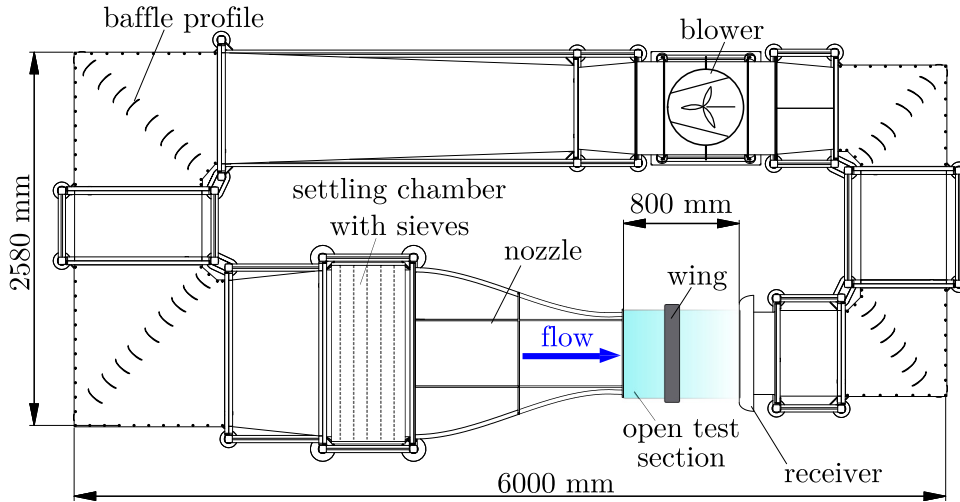


Fig. 2. Subsonic wind tunnel at PFS (Helmut-Schmidt University Hamburg).

by mounting the extra mass at different positions. Since the elastic axis is fixed for all cases it means that both points coincide in *case I*, whereas the c.o.g. is ahead or behind the e.a. for cases *II* and *III*, respectively.

Based on the aeroelastic theory the flutter stability depends on the position of the c.o.g. with respect to the elastic axis. A shift of the center of gravity towards the leading edge is increasing the flutter stability of the airfoil. Thus, *case II* is the most stable one, whereas *case III* is the most unstable configuration and *case I* should show an intermediate behavior between the two extremes. In general, flutter stability is characterized here by the minimum velocity at which flutter occurs. Consequently, the corresponding Reynolds number at flutter depends on the individual case. Furthermore, the behavior of limit-cycle oscillations within the investigated Re range also depends on the case studied.

The next section outlines the experimental setup including the wind tunnel, the model of the wing and the elastic mounting as well as the measurement techniques used to record the dynamic behavior of the wing.

3. Experimental setup

3.1. Wind tunnel

The experimental investigations of the flow around the elastically mounted airfoil are conducted in a Göttingen-type (closed loop) subsonic wind tunnel with an open test section of the dimensions 800 mm × 500 mm × 375 mm ($l \times w \times h$) shown in Fig. 2. The free-stream turbulence intensity is less than 0.5% over the whole velocity range of the wind tunnel ($u_{\max} = 28$ m/s).

3.2. Model of the wing

The investigation focuses on a 2-DOF system which is usually described as a two-dimensional problem, i.e., by the airfoil theory. In the experiment the NACA 0012 airfoil (chord length $c = 100$ mm) is represented by an unswept wing. The model of the rigid wing is made of poly-lactic acid (PLA) and manufactured by adhesive technology, i.e., printing. In order to reduce the weight the infill grading is set to 20% and the wing is printed in three parts which are added afterwards by means of a bonded joint to a final length of 600 mm. This length is motivated by the spanwise dimensions of the test section ($= 500$ mm) and results in an aspect ratio $l/c = 6$. In this configuration, the tips of the wing, where the elastic mounting is installed, are not exposed to the flow in order to minimize disturbances and the wing-tip effect. Furthermore, the wing is treated by a corrosive solution to produce a smooth surface leading to a mean surface roughness between $8.9 \mu\text{m} \leq R_a \leq 37.9 \mu\text{m}$ measured by a high-resolution digital microscope (Keyence VHX-6000). Subsequently carried out large-eddy simulations (De Nayer et al., 2020) have confirmed that the assumption of a smooth surface in the predictions is justified and leads to a close agreement between the measured and predicted data.

The overall mass of the wing without any further connections is $m_{w,0} = 0.181$ kg. The mounting devices are centered around the e.a. and possess a mass $m_{w,m} = 0.1202$ kg. Additionally, the two extra masses with an overall mass $m_{w,e} = 0.034$ kg can be installed at both ends of the wing at variable positions along the chord line to shift the c.o.g. according to cases *I*, *II* and *III*.

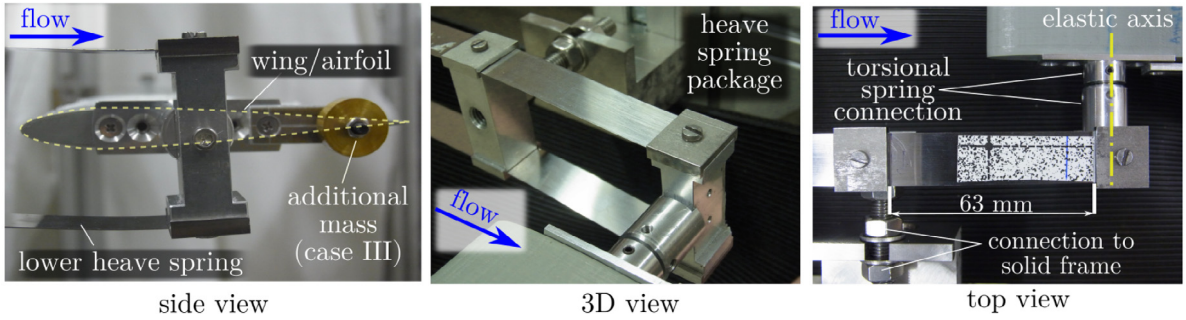


Fig. 3. Actual spring construction used for the elastic mounting of the wing in the test section.

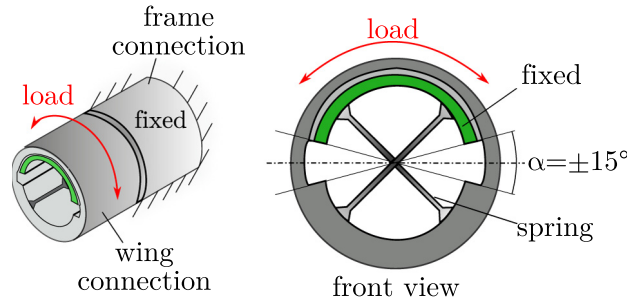


Fig. 4. Schematic representation of the torsional spring used for the realization of the rotational stiffness.

3.3. Elastic mounting

The actual construction of the utilized spring system is depicted in Fig. 3 showing only one side of the symmetrically mounted wing. In the side view (left) the elastically mounted airfoil and the connected extra mass (here shown for case III) are visible. The bending stiffness connected to the vertical motion of the wing is idealized by a doubled heave spring construction (middle), where one end is rigidly fixed to a solid frame by means of a screw connection. The details of the spring system are found in the right image: The free length of the heave springs is set to $l_h = 63$ mm ($l_h/c = 0.63$) leading to a stiffness of $k_h = 698$ N/m taking the spring systems at both ends of the wing into account as explained in Section 4. At the unsupported end of the heave spring package a connector for the torsional spring is mounted. The torsional spring itself is a special cylindrical, limited rotational bearing with a radial stiffness as depicted in Fig. 4. It is capable for maximum deflection angles between $\pm 15^\circ$ and exhibits a total stiffness of $k_\alpha = 0.3832$ N m/rad (taken from the specifications of the manufacturer with details found at C-Flex Bearing Co. Inc.¹) adding up both springs of the wing (left and right side). The torsional stiffness k_α is later used in the measurements of the 1-DOF pure pitch system in order to determine the mass moment of inertia $I_\alpha^E = k_\alpha / (2\pi f_\alpha)^2$ for each case (see Section 4) considering the natural eigenfrequency f_α of the rotational DOF determined based on the DIC measurements.

The elastic mounting including the wing $m_{w,0}$, the extra mass $m_{w,e}$ and the mounting devices $m_{w,m}$ possesses a total mass $m_w = 0.33521$ kg considering all parts involved in the dynamics of the 2-DOF system. The system under gravity does not exceed the linear characteristics of the applied springs. The initial position of the airfoil is set to a zero incidence angle $\alpha = 0^\circ$.

3.4. Configuration setups

As mentioned in Section 2, three configurations with altered mass distributions are considered. The setups used for the experimental measurements are depicted in Fig. 5. In general, the elastic axis is fixed at $0.417c$ with respect to the leading edge of the airfoil. At this position the torsional spring is connected to the heave spring of the airfoil. The following configurations are investigated: Fig. 5(a) illustrates case I with the extra mass connected at the position $0.22c$ from the leading edge. In this configuration it was intended that the c.o.g. and the e.a. coincide. However, due to inaccuracies during the additive prototyping, it turned out that $x_{EG}^I/c = 0.006 \approx 0$. Corresponding simulations (De Nayer et al., 2020) of the decay of motion of the 2-DOF free-oscillation tests in still air (see Section 5) confirmed this value. In case II (Fig. 5(b)) the c.o.g. is shifted upstream of the e.a. by adding the extra mass at the leading edge resulting in $x_{EG}^II/c \approx -0.022$. The

¹ <https://c-flex.com/pivot-bearings/>.

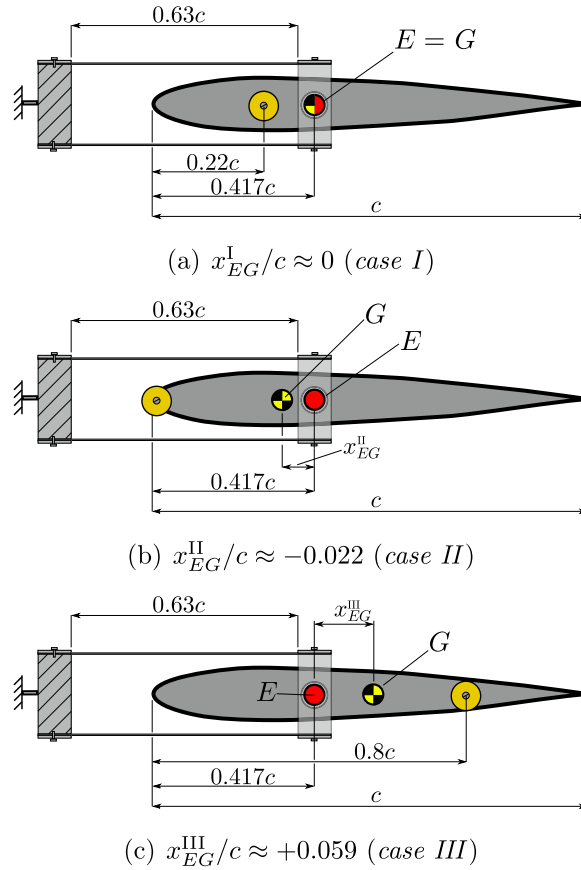


Fig. 5. Experimental configurations applied for the flutter analysis using different mass distributions in order to shift the center of gravity. The extra mass (yellow) is mounted at different distances from the leading edge: (a) upstream of the e.a. so that c.o.g. and e.a. coincide, e.g., $x_{EG}^I/c \approx 0$, (b) far upstream of the e.a. yielding $x_{EG}^{II}/c < 0$, and (c) far downstream of the e.a. yielding $x_{EG}^{III}/c > 0$. (For interpretation of the references to color in this figure legend, the reader is referred to the web version of this article.)

Table 1
Main parameters of all three configurations of the experimental setup.

Parameter	Symbol	Unit	Case I	Case II	Case III
Distance between c.o.g. and e.a.	x_{EG}/c	–	≈ 0	-0.022	$+0.059$
Mass moment of inertia based on f_α^{1-DOF}	I_α^E	kg m ²	1.399×10^{-4}	1.73×10^{-4}	1.73×10^{-4}
Mass of dynamic system	m_w	kg	0.33521	0.33521	0.33521
Bending stiffness	k_h	N/m	698	698	698
Torsional stiffness	k_α	N m/rad	0.3832	0.3832	0.3832
Total translational damping in still air	$b_h^{1-DOF,tot}$	N s/m	9.72×10^{-2}	8.57×10^{-2}	16.28×10^{-2}
Total rotational damping in still air	$b_\alpha^{1-DOF,tot}$	N m/s	3.70×10^{-5}	3.94×10^{-5}	4.54×10^{-5}
Total translational damping ratio in still air	$D_h^{1-DOF,tot}$	–	3.18×10^{-3}	2.80×10^{-3}	5.32×10^{-3}
Total rotational damping ratio in still air	$D_\alpha^{1-DOF,tot}$	–	2.53×10^{-3}	2.42×10^{-3}	2.79×10^{-3}

value is obtained by a balance of moments around the arising c.o.g. taking all masses ($m_{w,0}$, $m_{w,m}$ and $m_{w,e}$) into account. Based on the classic flutter theory this case is associated with an increased dynamic stability of the airfoil and thus higher free-stream velocities before flutter sets in. The third configuration (case III) is presented in Fig. 5(c) with the extra mass applied close to the trailing edge of the airfoil at $0.8c$ leading to $x_{EG}^{III}/c \approx +0.059$. Here, a decrease of the flutter stability in terms of lower flow velocities is expected. All basic parameters of the experimental setup connected to the elastic system are summarized in Table 1 for each configuration. To fully describe the system the damping parameters for both degrees of freedom are necessary. Similar to k_h and I_α^E these values are determined in Section 4 based on the measurements in the 1-DOF setup but are already listed in Table 1.

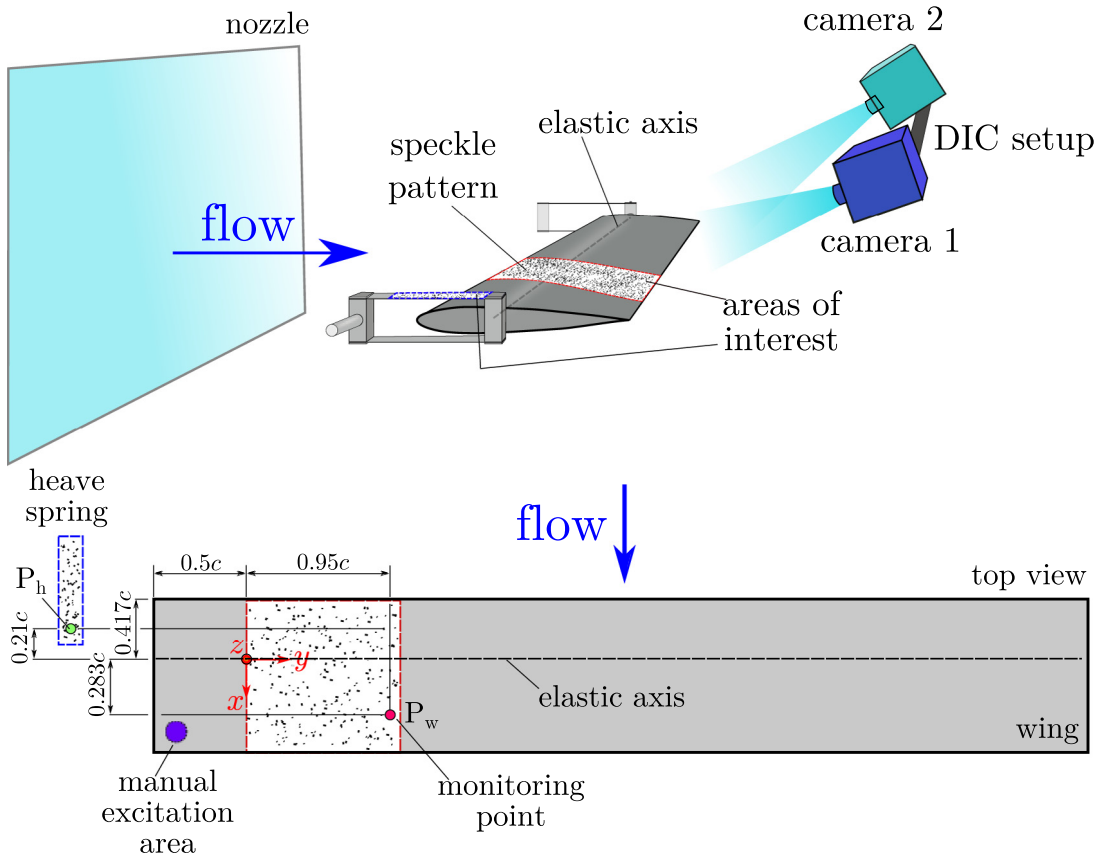


Fig. 6. Schematic representation of the DIC setup in the wind tunnel including the positions of the monitoring points on the heave spring P_h and on the wing P_w .

3.5. Measurement technique

The displacements Δz of the rigid wing in vertical direction are measured by the three-dimensional digital-image correlation (DIC) technique. It is based on a stereoscopic setup using two high-speed cameras (SpeedCam MacroVis EoSens). Since DIC is an optical method, it offers the advantage of contactless measurements with the capability of capturing large displacement fields. This feature makes it superior compared to laser-distance sensors or standard unidirectional displacement transducers, which are usually applied pointwise. In highly dynamic systems, such as the investigated elastically mounted wing, a non-invasive method is favored in order to exclude the influence of the measurement device on the system studied. However, the investigated geometry has to be in the visible range of the applied cameras. Furthermore, high-speed measurements require a strong light source in order to ensure a sufficient illumination for the short shutter times of the cameras. Another important aspect of DIC is the required speckle pattern, which is necessary to determine the displacements. This pattern has to be applied to the surface of the measured object. In a subsequent step a cross-correlation function is used to calculate the displacement vector by comparing the speckle patterns of two images taken at different instances in time. The accuracy of DIC is depending on the resolution of the applied cameras and the density of the speckle pattern. During the processing of the data the investigated area of the speckle pattern is discretized in a map consisting of so-called “sub-sets”. A sub-set is a region of $n \times n$ pixels used for the cross-correlation analysis. For present devices with modern sub-pixel algorithms the uncertainty of DIC lies in the magnitude of 0.01 pixel for in-plane measurements, which converts to physical units in the order of 10^{-6} m (Ke et al., 2011). Furthermore, the out-of-plane uncertainty is usually higher depending strongly on the quality of the calibration, i.e., the utilized calibration target, as discussed in Reu (2013). Usually a measurement accuracy in the magnitude of 0.1 pixel (10^{-4} m) is reached for the out-of-plane component. In the mean time DIC is widely used, e.g., to measure the three-dimensional deformations of highly flexible rotor blades (Sicard and Sirohi, 2013; Sirohi and Lawson, 2012). The actual setup is depicted in Fig. 6.

The cameras are mounted outside the test section close to the receiver of the wind tunnel not influencing the flow field. Schneider–Kreuznach Xenoplan lenses with a focal length of 22 mm are mounted to the cameras. These generate a field of view of about $0.25 \text{ m} \times 0.25 \text{ m}$. The calibration of the system yields a stereo angle between both cameras

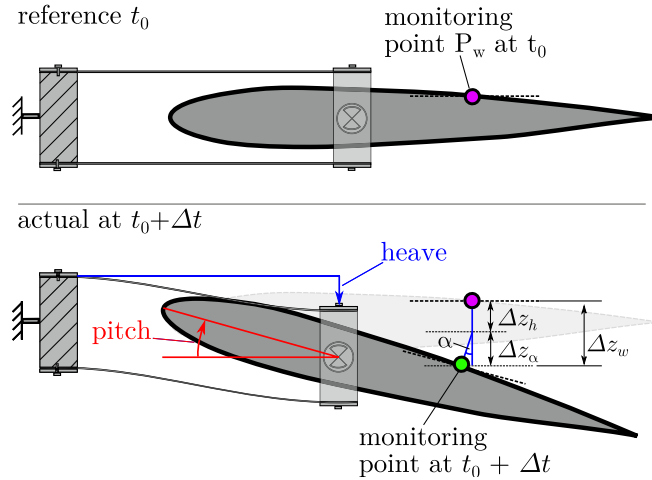


Fig. 7. Measurement of translation (heave) and rotation (pitch) in a single signal by DIC measurements of the measuring point P_w on the oscillating airfoil.

of 34.09° . The base-line vector, which marks the distance between both cameras, is set to 423.13 mm. A calibration residuum of 0.082 pixel is achieved, which indicates the average uncertainty of the found markers on the calibration target (DANTEC 11×11 mm high precision target). The calibrated system has a maximum uncertainty of measurement for each displacement component of $\Delta x_{\text{uncert}} \pm 0.003$ mm, $\Delta y_{\text{uncert}} \pm 0.004$ mm and $\Delta z_{\text{uncert}} \pm 0.006$ mm based on the maximum displacements (*case II*). The measurements are performed and controlled by the software VisArt.² The actual evaluation of the displacements Δz of each image-pair in vertical direction is calculated by the software Istra 4D³ using a sub-set size of 9×9 pixels. This translates to a physical size of 1.81×1.81 mm.

At first the oscillating wing is measured at a frame rate 250 fps with an image resolution of 1503×996 pixels taking only the monitoring point on the wing P_w into account. Thus, this series is denoted *single-point measurements* (see Section 6.1). This procedure inevitably leads to a data set, where the single degrees of freedom cannot be separated anymore. However, it is still possible to determine the frequency response as a major characteristic of the dynamic system based on the single-point DIC data. In this series the applied camera setting with an available memory of 8 GB per camera allows a data sample of 5611 double images covering a time span of 22.44 s.

In a second series denoted *two-point measurements* (see Section 6.2) the frame rate of the cameras is increased to 500 fps (camera setting: 1503×996 pixels, 5611 double images, 11.22 s) and focuses mainly on the details of the most interesting oscillations reached at specific Re numbers. For this purpose, a second monitoring point P_h on the heave spring is introduced in order to separate the displacements of heave and pitch accordingly by subtracting the pure heave from the wing displacements $\Delta z_\alpha = \Delta z_w - \Delta z_h$. This procedure has the advantage to isolate the heave DOF from the overall wing movement, which is used to determine the phase-shift angle φ between heave and pitch.

Due to the specific mounting, each camera focuses under a certain angle onto the speckle patterns, which are applied to the upper side of the one heave spring and the wing. Since the wing is unswept and the curvature of the NACA 0012 airfoil is moderate, both cameras observe the complete speckle pattern without hidden regions in the reference configuration. However, at a high negative angle of attack, i.e., downward pitch, the speckle pattern at the leading edge is not visible since the wing moves out of the camera view. Thus, the correlation area in which successful measurements are collected, is restricted to an effective region which limits the choice of potential monitoring points. The schematic top view of the wing in Fig. 6 depicts the exact position of the monitoring points. Each speckle pattern is digitally generated and printed onto a thin and smooth sheet of paper which is glued onto the heave spring and the wing by means of an adhesive bond to keep flow disturbances at a minimum. The speckles are covering an area fraction of 23% on the designated measurement fields on the wing and the heave spring with speckle diameters d_{sp} ranging between $0.17 \text{ mm} \leq d_{sp} \leq 0.47 \text{ mm}$. The frame of reference is located on the elastic axis with a distance of $0.5c$ from the left side of the wing. The wing monitoring point $P_w(0.283c/0.95c/0c)$ is used to measure the total displacements $\Delta z_w(t)$ in vertical direction which are considered to capture the main characteristics of the translational and rotational movement of the airfoil in a single signal illustrated in Fig. 7. As mentioned above the measured DIC signal of P_w contains the information on both degrees of freedom, i.e., the heave and pitch frequency. Furthermore, damping and excitation phenomena are measured in the complete Re number range for each case.

² <http://www.hsvision.de/en/products/software/visart-detail>.

³ <https://www.dantecdynamics.com/istra-4d-shearography>.

In DIC an undeformed reference configuration is necessary to which all other images of a measurement are compared in order to determine the displacements. In the present case the reference configuration at t_0 is the airfoil in idle position at an angle of attack of $\alpha = 0^\circ$. At any other time step $t_0 + \Delta t$ the displacements Δz_w are determined by a cross-correlation algorithm of the speckle pattern between the reference and the actual image. The observed monitoring point P_w of the reference configuration (magenta in Fig. 7) has moved to its actual location (green) due to the heave displacement Δz_h and the pitch displacement Δz_α , which are recorded in the *single-point measurements* as a combined displacement Δz_w .

Nevertheless, a separate view of the heave and pitch motion is necessary to investigate the LCO behavior and the corresponding phase-shift angle φ between translation and rotation of the wing at each configuration. For this purpose, a second measurement of these special cases with increased temporal resolution is carried out taking the monitoring point P_h on the heave spring in form of the *two-point measurements* into account as mentioned above. This procedure leads to a small error due to the fact that the measurements of the heave motion are not taken directly at the position of the elastic axis. The maximum relative error is calculated by $|\Delta z_{h, \text{error}}^{\text{max}} / \Delta z^{\text{max}}| \cdot 100\% \approx 6\%$. The source of this error is discussed in detail in Appendix.

4. Determination of parameters by free-oscillation tests with 1-DOF in still air

Free-oscillation tests in still air considering the 1-DOF (heave or pitch) system are carried out to measure the natural eigenfrequencies f_h (vertical translation) and f_α (rotation) of the elastic system. From these measurements the mass moment of inertia $I_\alpha^E = k_\alpha / (2\pi f_\alpha)^2$, the bending stiffness $k_h = (2\pi f_h)^2 m_w$, the total damping coefficients $b_h^{\text{tot}} = 2D_h^{\text{tot}} \sqrt{k_h m_w}$ and $b_\alpha^{\text{tot}} = 2D_\alpha^{\text{tot}} \sqrt{k_\alpha I_\alpha^E}$ using its corresponding total damping ratios D_h^{tot} and D_α^{tot} are analytically determined. It is important to note that the damped system refers to the total amount of damping including the material damping from the springs and the damping induced by the surrounding fluid. For coupled numerical simulations of the system solely the material damping is required for the structural solver, since the damping by the surrounding air is accounted for directly. For details on how to deal with this lack of data refer to De Nayer et al. (2020).

Note that for the cases discussed in the following subsections the displacements of the heave motion were low-pass filtered. In the experiments a minor oscillation around the x -axis (rolling motion) could not be completely excluded due to the three-dimensional nature of the setup. According to the feasible field of view of the DIC-system as well as the chosen size and position of the speckle pattern, the effect of the third DOF cannot be adequately resolved. Nevertheless, the data indicate that this oscillation rapidly damps out after the initial disturbance of the wing leaving the major part of the remaining oscillations to the main DOF, i.e., heave. Since the frequency of the rolling motion is at about 11.3 Hz, it is well above the eigenfrequency of the heave motion and can be filtered out.

4.1. Case I: $x_{EG}^I/c \approx 0$

The DIC measurements of *case I* are depicted in Fig. 8 showing the vertical displacement Δz of the monitoring point P_w after a manually applied excitation of the wing.

Fig. 8(a) presents the history of the displacements for the 1-DOF system, where only the heave motion is enabled, while the rotation is blocked mechanically. These data provide the decay of the translational motion in a time span of 22.44 s. They are used to calculate the total damping ratio $D_h^{\text{I,tot}} = \Lambda / 2\pi = 3.18 \times 10^{-3}$ from the logarithmic decrement $\Lambda = (1/n) \ln[(\Delta z(t)_1 / \Delta z(t)_{1+n})]$ ($n = 20$, based on the amplitudes of the peak values $\Delta z(t)$ for each period taken between $4 \text{ s} \leq t \leq 6.8 \text{ s}$). Furthermore, the natural eigenfrequency $f_h^{\text{I-DOF,I}} = 7.26 \text{ Hz}$ of the pure heave motion is determined by a fast Fourier transform (FFT) depicted in Fig. 8(b). This frequency is used to calculate the bending stiffness of the elastic system yielding $k_h = 698 \text{ N/m}$.

The analogous procedure is applied for the pure pitch motion shown in Figs. 8(c) and 8(d). Here, a lower total damping ratio of $D_\alpha^{\text{I,tot}} = 2.53 \times 10^{-3}$ is found along with a natural eigenfrequency $f_\alpha^{\text{I-DOF,I}} = 8.33 \text{ Hz}$ revealing a lower damping of the rotational motion. Moreover, by using the measured frequency of the rotation $f_\alpha^{\text{I-DOF,I}}$ the mass moment of inertia for this case is found at $I_\alpha^{\text{I}} = 1.399 \times 10^{-4} \text{ kg m}^2$.

4.2. Case II: $x_{EG}^{II}/c \approx -0.022$

The results of the second case are depicted in Fig. 9. The heave frequency $f_h^{\text{II-DOF,II}} = 7.26 \text{ Hz}$ of the 1-DOF setup (see Fig. 9(b)) is identical to *case I*, since the relevant parameters for the translatory motion (total mass and translational spring constant) are unchanged. Due to the relocation of the extra mass towards the leading edge, the mass moment of inertia increases to $I_\alpha^{\text{II}} = 1.73 \times 10^{-4} \text{ kg m}^2$. This is noticed by the decrease of the pitch frequency $f_\alpha^{\text{II-DOF,II}} = 7.49 \text{ Hz}$ compared with the first configuration visible in Fig. 9(d). The time histories in Figs. 9(a) and 9(c) are again used to determine the total damping ratios which yield $D_h^{\text{II,tot}} = 2.80 \times 10^{-3}$ for the heave and $D_\alpha^{\text{II,tot}} = 2.42 \times 10^{-3}$ for the pitch motion. Obviously, the total damping ratios for *case I* and *II* are not identical, but the maximum deviations are about 10%, which is acceptable.

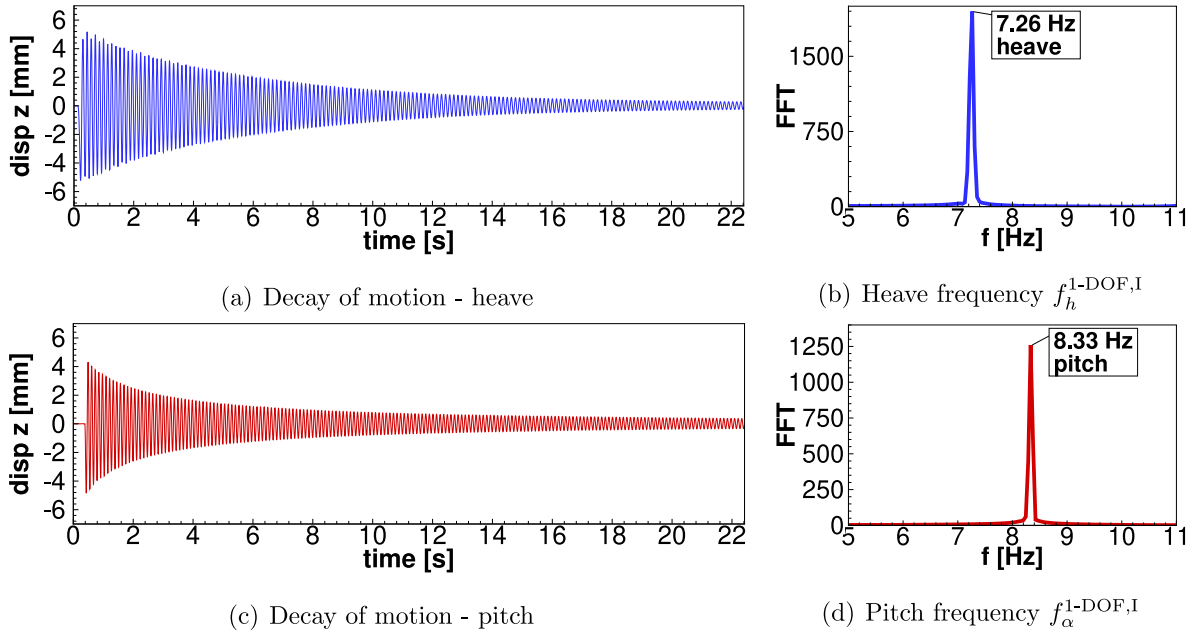


Fig. 8. Case I: DIC measurements at P_w of the free-oscillation tests in still air for the 1-DOF system (heave or pitch).

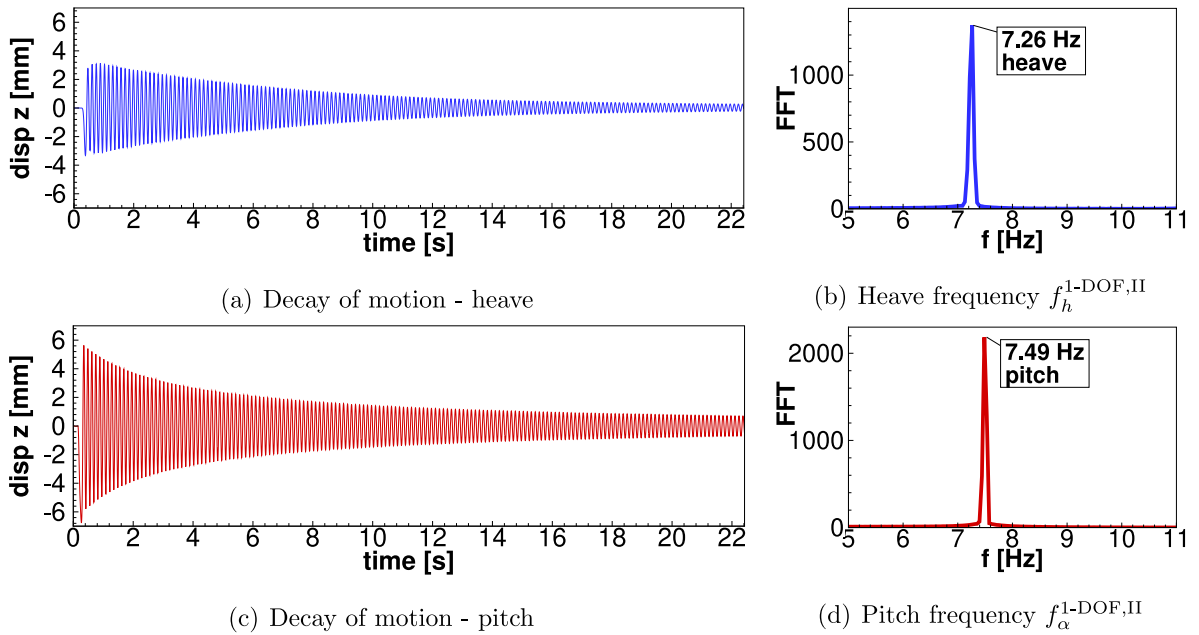


Fig. 9. Case II: DIC measurements at P_w of the free-oscillation tests in still air for the 1-DOF system (heave or pitch).

4.3. Case III: $\chi_{EC}^{III}/c \approx +0.059$

In the third case the extra mass is mounted close to the trailing edge of the airfoil. The corresponding measurements are depicted in Fig. 10. As in the former cases the heave frequency of the 1-DOF system is found at $f_h^{1-DOF,III} = 7.26$ Hz (see Fig. 10(b)). Since the absolute value of the distance between the extra mass and the elastic axis in case III is similar to case II, the pitch frequency does not change significantly and remains at $f_\alpha^{1-DOF,III} = 7.49$ Hz (Fig. 10(d)). Thus, the mass moment of inertia is approximately identical to case II. Astonishingly, the total damping ratio of the heave motion $D_h^{III,tot} = 5.32 \times 10^{-3}$ is about two times larger than in the other configurations. Since the spring system is still the same,

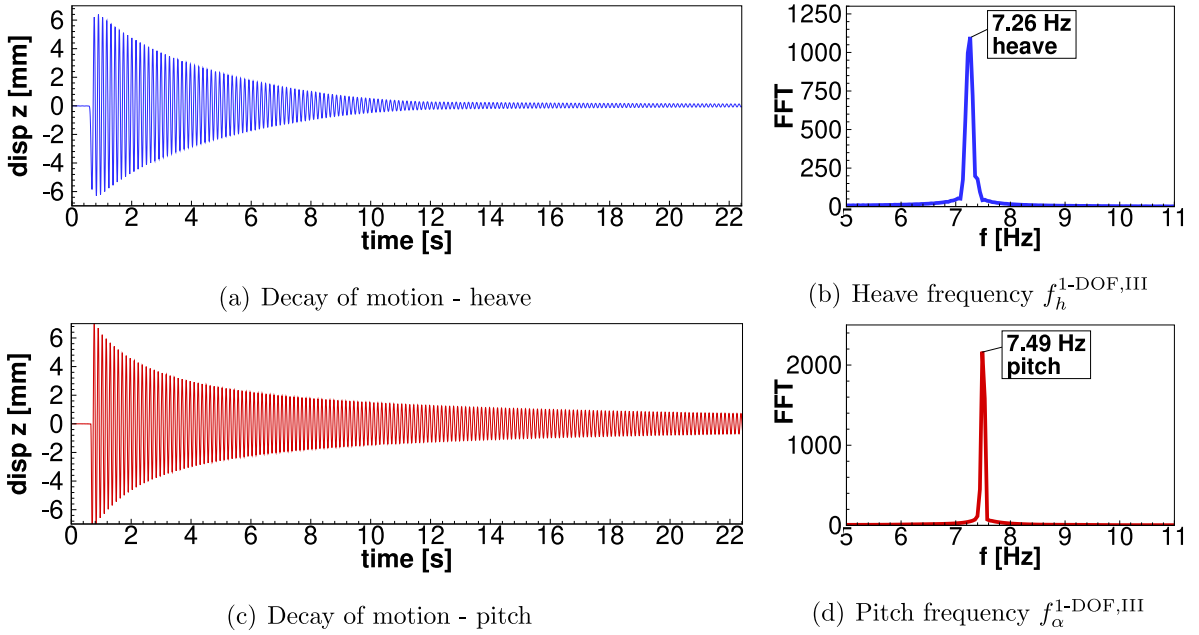


Fig. 10. Case III: DIC measurements at P_w of the free-oscillation tests in still air for the 1-DOF system (heave or pitch).

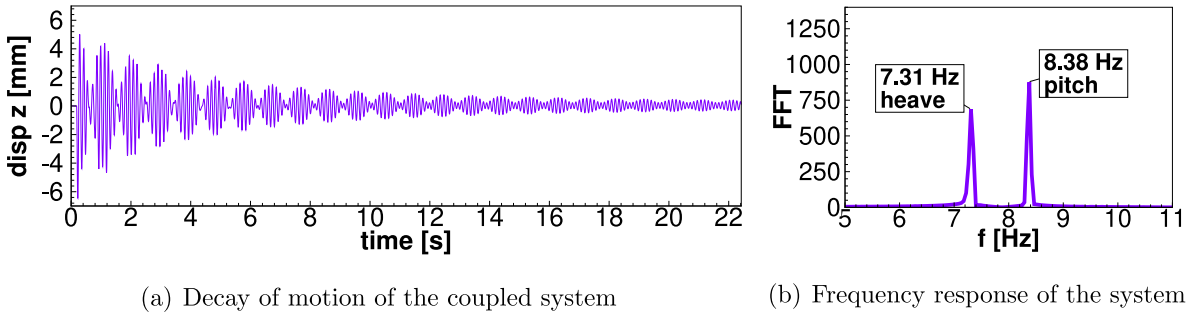


Fig. 11. Case I: DIC measurements at P_w of the free-oscillation tests in still air for the coupled 2-DOF system (heave and pitch).

the pure structural damping is expected to stay more or less constant. Consequently, the first idea to attribute the increase of the total damping ratio to an increased damping by the surrounding fluid. This possibility was investigated in the corresponding simulations (De Nayer et al., 2020) and could be excluded. Since the experiment is reproducible and thus an error can be excluded, presently no final explanation can be provided. One option is that due to larger spring deformations in this case, some elastic dissipation occurs. This behavior is not observed for the decay of the rotational motion yielding a damping ratio of $D_{\alpha}^{ll,tot} = 2.79 \times 10^{-3}$ comparable to cases I and II.

In the following sections the characteristic behavior of the system in the 2-DOF setup (heave and pitch) is discussed. The analysis is subdivided into free-oscillation tests in still air and the system under wind load.

5. Free-oscillation characteristics with 2-DOF in still air

5.1. Case I: $x_{EG}^I/c \approx 0$

The 2-DOF system of case I (Fig. 11) exhibits similar eigenfrequencies as the 1-DOF measurements with a heave frequency $f_h^{2-DOF,I} = 7.31$ Hz and a pitch frequency $f_{\alpha}^{2-DOF,I} = 8.38$ Hz shown in Fig. 11(b). Both frequencies are slightly higher than observed in the 1-DOF cases. The difference of both frequencies $\Delta f^{2-DOF,I} = 1.07$ Hz is the so-called “beat frequency” causing the characteristic decay of motion in form of a wave depicted in the temporal domain in Fig. 11(a). Theoretically, both DOF should be uncoupled in this configuration at least in vacuum, since the elastic axis coincides with the center of gravity. However, due to the imperfect superposition of the elastic axis and the center of gravity arising from manufacturing tolerances of the wing (see Section 3.4) a slight inertial coupling between heave and pitch still remains.

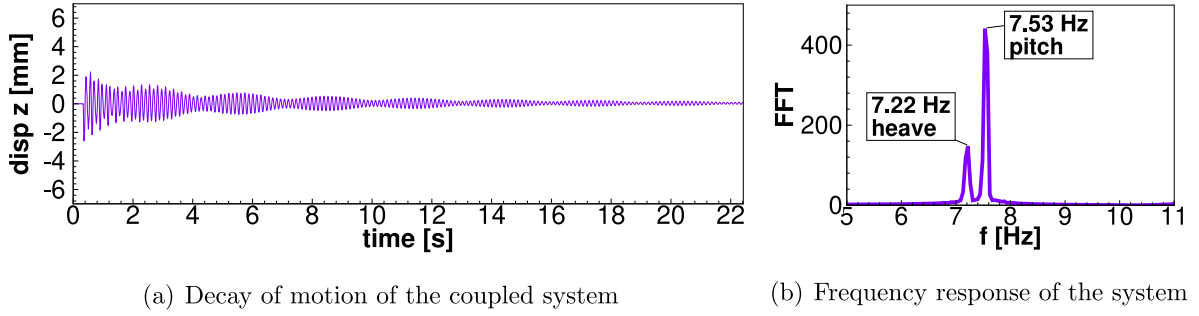


Fig. 12. Case II: DIC measurements at P_w of the free-oscillation tests in still air for the coupled 2-DOF system (heave and pitch).

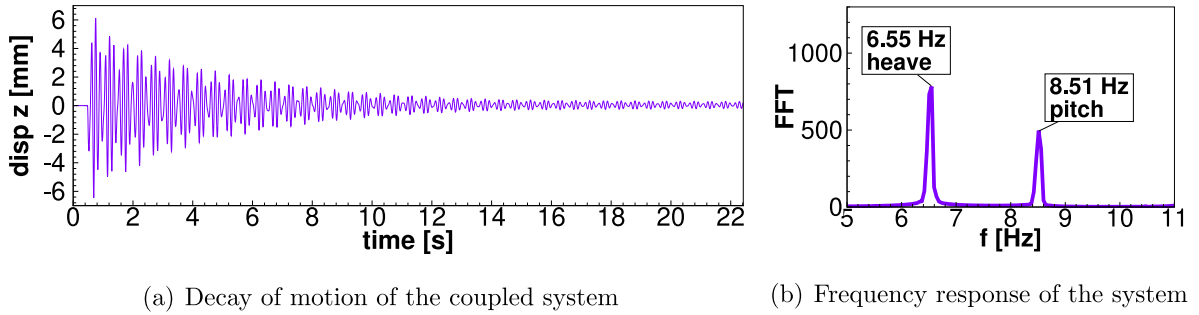


Fig. 13. Case III: DIC measurements at P_w of the free-oscillation tests in still air for the coupled 2-DOF system (heave and pitch).

The actual value of x_{EG}/c is determined based on corresponding numerical simulations (De Nayer et al., 2020) of the identical case. By variation of x_{EG}/c a best fit between the experimental data and the numerical predictions is found at a positive value of $x_{EG}/c \approx 0.006$. The effect of inertial coupling at positive values of x_{EG}/c is presented in a recent study by Boudreau et al. (2020) discussing the potential of a flapping foil as a renewable energy source. Larger values of x_{EG}/c yielding an increasing static moment lead to a stronger inertial coupling. That allows an increased efficiency for energy harvesting. Interestingly, the numerical simulations (De Nayer et al., 2020) also reveal a weak coupling between both DOF at $x_{EG}/c = 0$. The coupling of both DOF vanishes in case of simulations without surrounding fluid, i.e., in a vacuum setup. In this case, both DOF oscillate independently. In conclusion, a system which is uncoupled at $x_{EG}/c = 0$ in vacuum is no longer fully uncoupled if the surrounding air contributes to the energy transfer between both DOF. Thus, both effects, i.e., the imperfect setup and the presence of the surrounding fluid, play a role for the periodic exchange of energy observed in the experimental setup. While passing energy from one mode to the other, the system exhibits periods of almost complete cancellation of motion seen in the amplitude of the displacements. However, the frequency ratios $f_h^{1-DOF,I}/f_\alpha^{1-DOF,I} = f_h^{2-DOF,I}/f_\alpha^{2-DOF,I} = 0.872$ between 1-DOF and 2-DOF are identical.

5.2. Case II: $x_{EG}^{II}/c \approx -0.022$

In this case the beat frequency of the 2-DOF system is $\Delta f^{2-DOF,II} = 0.31$ Hz and thus lower than in case I. The frequencies of heave and pitch are very close to each other, $f_h^{2-DOF,II} = 7.22$ Hz and $f_\alpha^{2-DOF,II} = 7.53$ Hz (see Fig. 12(b)). Consequently, the period between the modal energy transfer is larger as visible in Fig. 12(a). Furthermore, the eigenfrequencies of the 2-DOF system are slightly altered compared to the 1-DOF tests. Nevertheless, the frequency ratio of the 1-DOF $f_h^{1-DOF,II}/f_\alpha^{1-DOF,II} = 0.969$ is close to the 2-DOF system with $f_h^{2-DOF,II}/f_\alpha^{2-DOF,II} = 0.959$.

5.3. Case III: $x_{EG}^{III}/c \approx +0.059$

The 2-DOF case reveals a remarkably different oscillation characteristic (see Fig. 13) compared to case II, although the eigenfrequencies of the 1-DOF tests are identical (see Figs. 9 and 10).

The beat frequency $\Delta f^{2-DOF,III} = 1.96$ Hz is higher resulting in a rapid transfer of modal energy between pitch and heave. As a consequence, the eigenfrequencies of translation and rotation are further apart with a heave frequency $f_h^{2-DOF,III} = 6.55$ Hz and a pitch frequency $f_\alpha^{2-DOF,III} = 8.51$ Hz. Obviously, the frequency ratio $f_h^{1-DOF,III}/f_\alpha^{1-DOF,III} = 0.969$ of the 1-DOF system differs significantly from the 2-DOF system with $f_h^{2-DOF,III}/f_\alpha^{2-DOF,III} = 0.770$. This particular feature makes case III very interesting for numerical predictions in order to receive a deeper insight into the phenomenon.

Table 2

Frequencies obtained by the free-oscillation tests in still air.

Parameter	Symbol	Unit	Case I	Case II	Case III
Translation eigenfrequency 1-DOF	f_h^{1-DOF}	Hz	7.26	7.26	7.26
Rotational eigenfrequency 1-DOF	f_α^{1-DOF}	Hz	8.33	7.49	7.49
Translation eigenfrequency 2-DOF	f_h^{2-DOF}	Hz	7.31	7.22	6.55
Rotational eigenfrequency 2-DOF	f_α^{2-DOF}	Hz	8.38	7.53	8.51
Frequency difference 2-DOF	Δf^{2-DOF}	Hz	1.07	0.31	1.96
Frequency ratio 1-DOF	$f_h^{1-DOF} / f_\alpha^{1-DOF}$	–	0.872	0.969	0.969
Frequency ratio 2-DOF	$f_h^{2-DOF} / f_\alpha^{2-DOF}$	–	0.872	0.959	0.770

Table 3

Free-stream velocity and Re number range for each case.

U_∞ [m s ⁻¹]	Re	Case
1.44	9.66×10^3	I–III
2.46	1.65×10^4	I–III
3.56	2.39×10^4	I–III
4.56	3.06×10^4	I, III
5.06	3.39×10^4	III
5.37	3.60×10^4	I
6.99	4.69×10^4	II
13.08	8.77×10^4	II

All relevant frequencies of the free-oscillation tests (1-DOF and 2-DOF) in still air for all three configurations are summarized in Table 2. The next section focuses on the dynamic behavior of each configuration as a 2-DOF system under wind load.

6. Free-oscillation characteristics with 2-DOF under wind load

Switching from the fluid at rest to the flow situation with a constant free-stream velocity, this section outlines the dynamic behavior of all three configurations of the 2-DOF system. The discussion follows an analogous manner as the free-oscillation tests in still air. The free-stream velocities investigated for each case are given in Table 3.

At the beginning of each measurement the airfoil was exposed to the targeted free-stream velocity. After a brief settling period the measurement was carried out starting with a manually introduced excitation applied at the designated point on the wing (see Fig. 6). After this initial disturbance the airfoil oscillated freely under the influence of the wind load. These tests considered the single monitoring point P_w on the wing. The data are used to determine the frequency response in order to characterize the dynamic characteristics at each Re. This is followed by a detailed investigation on the limit-cycle oscillations and the flutter phenomenon relying on two monitoring points (P_w and P_h). The respective oscillations mainly occurred at a specific free-stream velocity. Here, especially the phase shift between the vertical heave displacement and the pitch angle is an interesting property obtained by the simultaneous measurement at the two monitoring points.

6.1. Single-point measurements at the monitoring point P_w

6.1.1. Case I: $x_{EG}^l/c \approx 0$

The vertical displacements and the corresponding frequency responses of case I are depicted in Fig. 14 focusing at five free-stream velocities in the range $9.66 \times 10^3 \leq \text{Re} \leq 3.60 \times 10^4$ ($1.44 \text{ m/s} \leq U_\infty \leq 5.37 \text{ m/s}$). Fig. 14(a) depicts the decay of motion after the initial excitation at $\text{Re} = 9.66 \times 10^3$. Due to the moderate flow velocity the history of the displacements are similar to the 2-DOF free oscillations in still air. However, the displacements are already damped to a minimum at about $t = 16 \text{ s}$. This stronger damping is also present in the frequency response in Fig. 14(b). Here, the FFT peak values of the pitch and heave frequency are significantly reduced compared with the still-air case (note the different scalings of both plots). The pitch frequency is slightly reduced to 8.33 Hz, whereas the heave frequency remains unchanged. At the next higher Re number (1.65×10^4) the damping effect of the wind load is even more pronounced leading to a quicker decay of the motion (Fig. 14(c)) with lower peak values of the FFT (Fig. 14(d)). Moreover, the frequencies of both DOF are approaching each other with an increased heave frequency (7.35 Hz) and a further decreased pitch frequency (8.24 Hz). By further rising the free-stream velocity, the time history at $\text{Re} = 2.39 \times 10^4$ in Fig. 14(e) indicates that the energy transfer between heave and pitch is no longer the same as before. In this case a strongly damped heave motion is observed. After about $t = 2 \text{ s}$ the pitch motion is mainly present and further damped until $t = 10 \text{ s}$. After the initial disturbance is damped out, small-amplitude oscillations (SAO) remain in the signal.

It is assumed⁴ that the SAO is caused by laminar separation of the boundary layer close to the trailing edge of the airfoil as discussed in Poirel et al. (2008) and Poirel and Mendes (2014). The frequency spectrum in Fig. 14(f) shows a broad

⁴ Supported by complementary numerical predictions, see De Nayer et al. (2020).

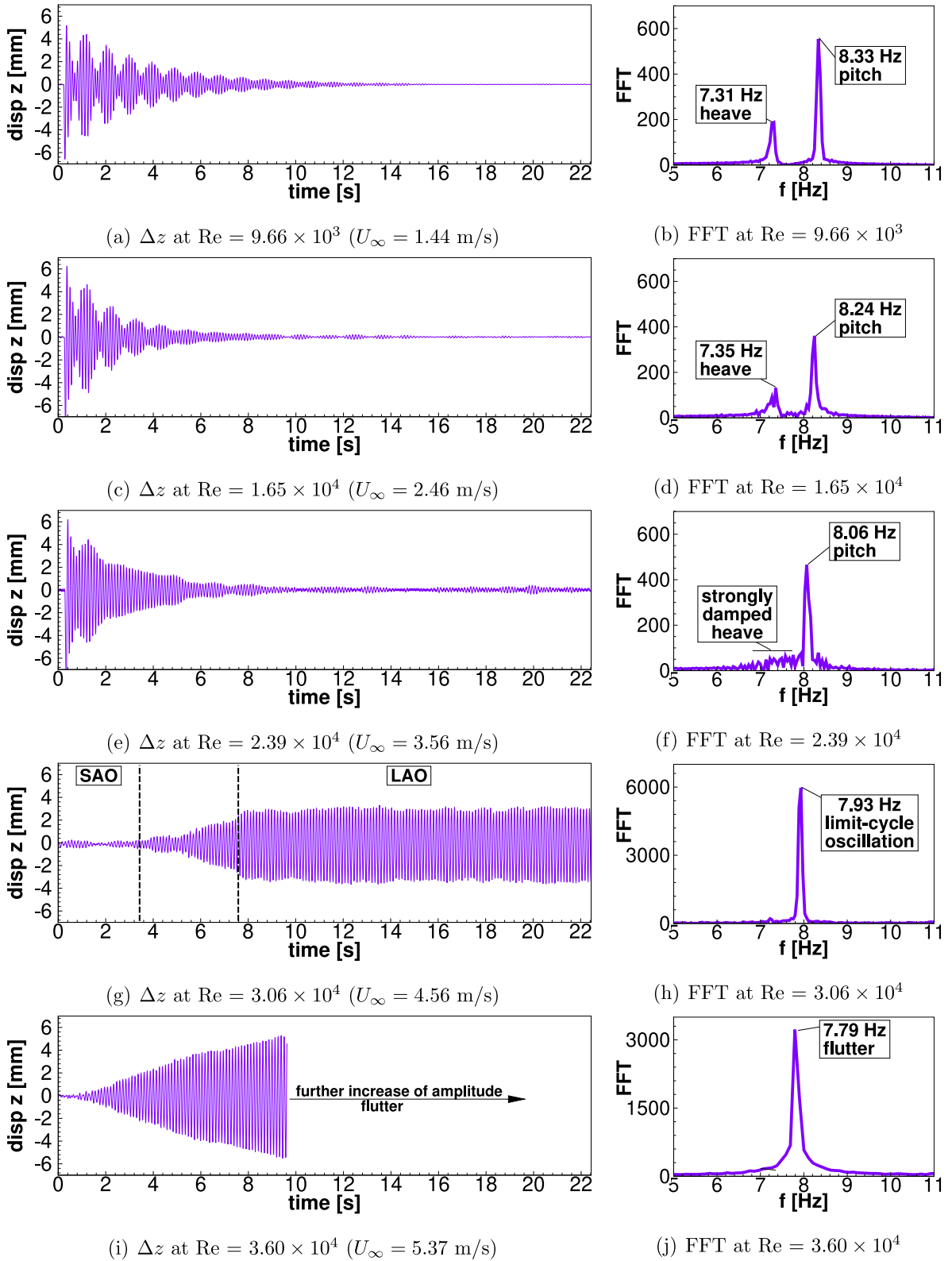


Fig. 14. Case I: DIC measurements at P_w : Time history and frequency response of the motion after a manually introduced disturbance (except for the last two cases) in the Re range $9.66 \times 10^3 \leq Re \leq 3.60 \times 10^4$ (1.44 m/s $\leq U_\infty \leq 5.37$ m/s).

frequency range between 6.5 Hz and 7.5 Hz corresponding to the heave frequency without a pronounced peak visible. The pitch frequency is further reduced to 8.06 Hz, but remains at a comparable FFT peak value as before. With a further increase of the free-stream velocity, i.e., $Re = 3.06 \times 10^4$, a limit-cycle oscillation occurs. In this case no initial disturbance is necessary to trigger this feature as apparent in Fig. 14(g). The growth in amplitude sets in after about 4 s, where small amplitude oscillations comparable to the previous Re number are visible from the beginning of the measurement. After exceeding this instant in time the amplitudes rise and settle at a much larger and constant peak-to-peak displacement of about $\Delta z = \pm 3.5$ mm according to a large-amplitude oscillation (LAO). Looking at the series of images of the DIC measurements, it is clear that the pitching motion of the airfoil is larger than the heave resulting in a clearly isolated frequency found at 7.93 Hz.

At the final free-stream velocity ($Re = 3.60 \times 10^4$) an exponential growth of the amplitudes of the airfoil associated with flutter is observed in the measurements as shown in Fig. 14(i). Both DOF are active resulting in a flutter frequency of 7.79 Hz. After about $t = 10$ s the measurement had to be stopped manually in order to prevent damaging the delicate spring system.

6.1.2. Case II: $x_{EG}^{II}/c \approx -0.022$

The DIC measurements of the second case are depicted in Fig. 15. The time history of the displacements and the corresponding frequency responses at $Re = 9.66 \times 10^3$ are shown in Figs. 15(a) and 15(b). The history of the vertical displacement follows the trend of the 2-DOF free-oscillation test. Again, the wind load has a damping effect on the initial disturbance visible in the decay of the motion, which has already ceased at about $t = 11$ s. The heave frequency is seemingly unchanged (7.21 Hz), whereas the pitch frequency is increased to 7.58 Hz. Similar to case I both frequencies exhibit a decrease in the corresponding FFT peaks compared to the free oscillations in still air. This trend continues in the measurement of the next higher Re presented in Fig. 15(c). A further rise of the damping is present, where the starting disturbance vanishes after $t = 8$ s. Both frequencies have changed to lower values, i.e., 7.13 Hz (heave) and 7.53 Hz (pitch) associated with lower peaks found in the FFT (Fig. 15(d)). An interesting development of the decay characteristics is present at $Re = 2.39 \times 10^4$ (Fig. 15(e)) and $Re = 4.69 \times 10^4$ (Fig. 15(g)). First, the initial excitations lead to amplified oscillations compared to the two lower Re numbers. Second, this is accompanied with an enlarged beat frequency since heave and pitch responses drift apart from $\Delta f = 0.53$ Hz at $Re = 2.39 \times 10^4$ (Fig. 15(f)) to $\Delta f = 1.02$ Hz at $Re = 4.69 \times 10^4$ (Fig. 15(h)). The alteration towards greater values of the difference between the heave and pitch frequency is a clear indicator for an increased flutter stability of the airfoil. Thus, the wind load causes a fluid-induced stiffness. This is supported by the heave and pitch peak values of the FFT, which more or less remain at the same level (see Figs. 15(f) and 15(h)) although there is a large difference between the free-stream velocities changing from 3.56 m/s to 6.99 m/s.

For the final case the free-stream velocity was significantly raised ($Re = 8.77 \times 10^4$) in order to receive the time history in Fig. 15(i) and the corresponding frequency responses in Fig. 15(j). Here, SAO are present in the time span $0 \leq t \leq 0.6$ s until the manually introduced excitation of the wing is applied. This superimposed deflection leads to a sudden change in the amplitude and the further evolution of the displacements is characterized by LAO. In the present measurement the LAO oscillates around a mean displacements of about $\overline{\Delta z} \approx 3$ mm in positive vertical direction due to a positive angle of attack. Since the airfoil is symmetric, the mean deflection can also be negative, i.e., the airfoil exhibits a negative angle of attack under this circumstance. The actual state (positive or negative α) depends on minor deviations in the initial setting of the airfoil ($\alpha \approx 0^\circ$) at rest or strong fluid-induced excitations due to flow separation at this free-stream velocity. The intense “flapping” motion of the airfoil was stopped manually after 13 s in order to avoid the damage of the setup. The frequency response reveals a remarkable frequency peak at 4.84 Hz associated with the LAO “flapping” type of motion. This frequency is lower than any of the former pitch or heave frequencies. A similar effect was found in Poirel and Mendes (2014), where a sudden jump from SAO to LAO is observed at comparable Re numbers and heave stiffnesses. The first harmonic of the LAO frequency is found at 9.61 Hz. The presence of the SAO during the initial time span $0 \leq t \leq 0.6$ s remains visible as a less pronounced peak located at about 7.65 Hz. This peak region is magnified on an extra ordinate in Fig. 15(j) in order to visualize it accordingly. This was verified by a separate FFT taking only the first 0.6 s of the signal before the LAO sets in into account in order to separate the SAO frequency. This issue will be discussed in detail in Section 6.2.2.

6.1.3. Case III: $x_{EG}^{III}/c \approx +0.059$

Fig. 16 depicts the results of the third case with the extra mass applied behind the elastic axis. As previously discussed for the 2-DOF free oscillations in still air, the frequency responses of heave and pitch reveal a different behavior compared to case II, although the total mass and the moment of inertia around the elastic axis I_α^E have not changed as outlined in Section 4. The characteristic motion of the decay and the frequencies contained in the signal at $Re = 9.66 \times 10^3$ are shown in Figs. 16(a) and 16(b). Both are in close agreement with the still-air case (Fig. 13), but similar to the previous two configurations the wind load has a damping effect on the initial excitation. However, after the disturbance has ceased, the airfoil remains oscillating at small but constant amplitudes indicated in the close-up view in Fig. 16(a). This phenomenon is not observed in case I and II. In Fig. 16(b) the frequency of the heave motion remains unchanged at 6.55 Hz and the pitch frequency is slightly shifted to 8.55 Hz compared to the still-air case (see Fig. 13). Due to the damping effect of the wind load, the peak values of the FFT are reduced. A similar dynamic behavior of the airfoil is present at $Re = 1.65 \times 10^4$ depicted in Figs. 16(c) and 16(d). A stronger damping of the heave motion is seen in the spectral domain but without

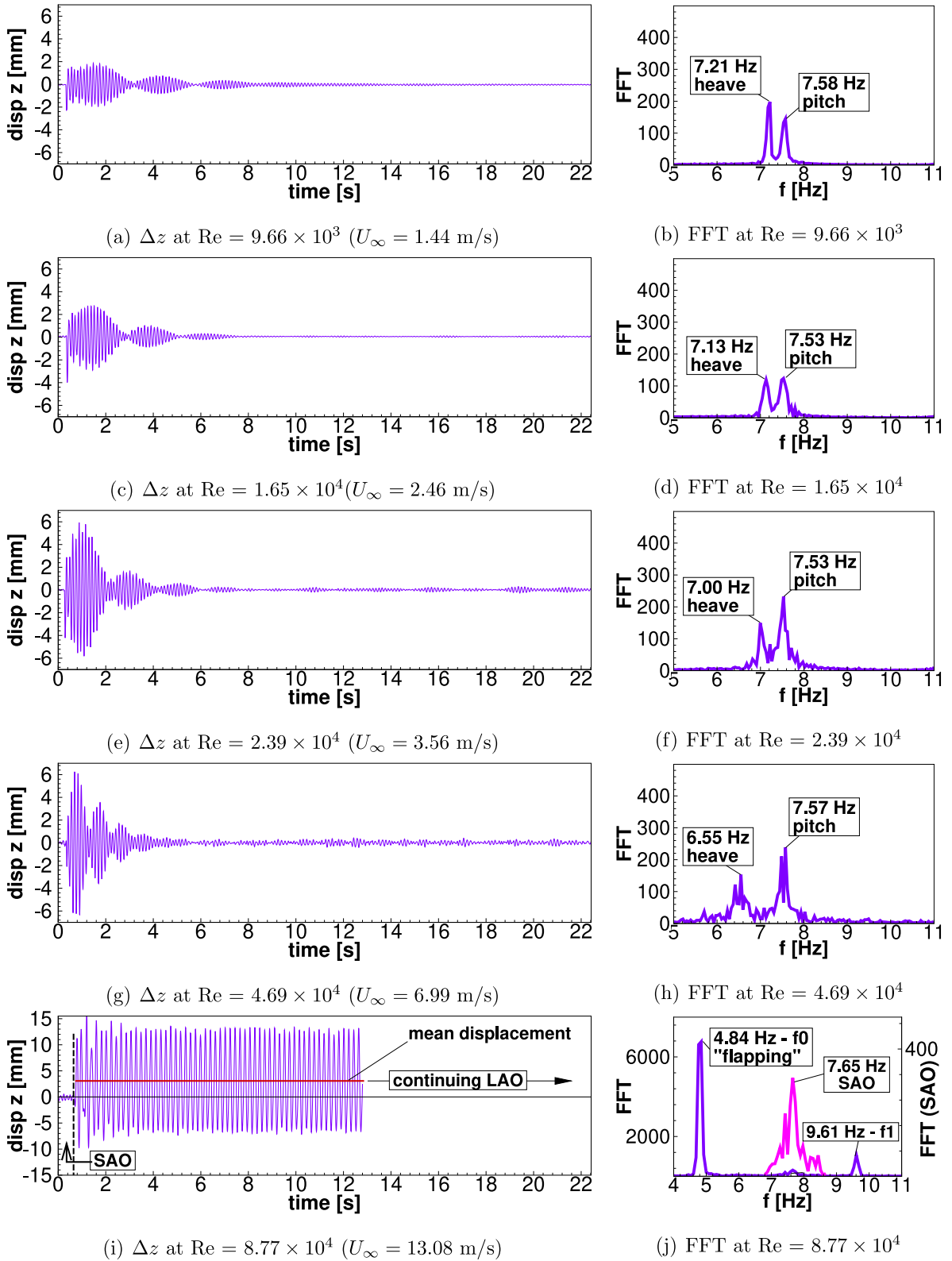


Fig. 15. Case II: DIC measurements at P_w : Time history and frequency response of the motion after a manually introduced disturbance in the Re range $9.66 \times 10^3 \leq Re \leq 8.77 \times 10^4$ (1.44 m/s $\leq U_\infty \leq 13.08$ m/s).

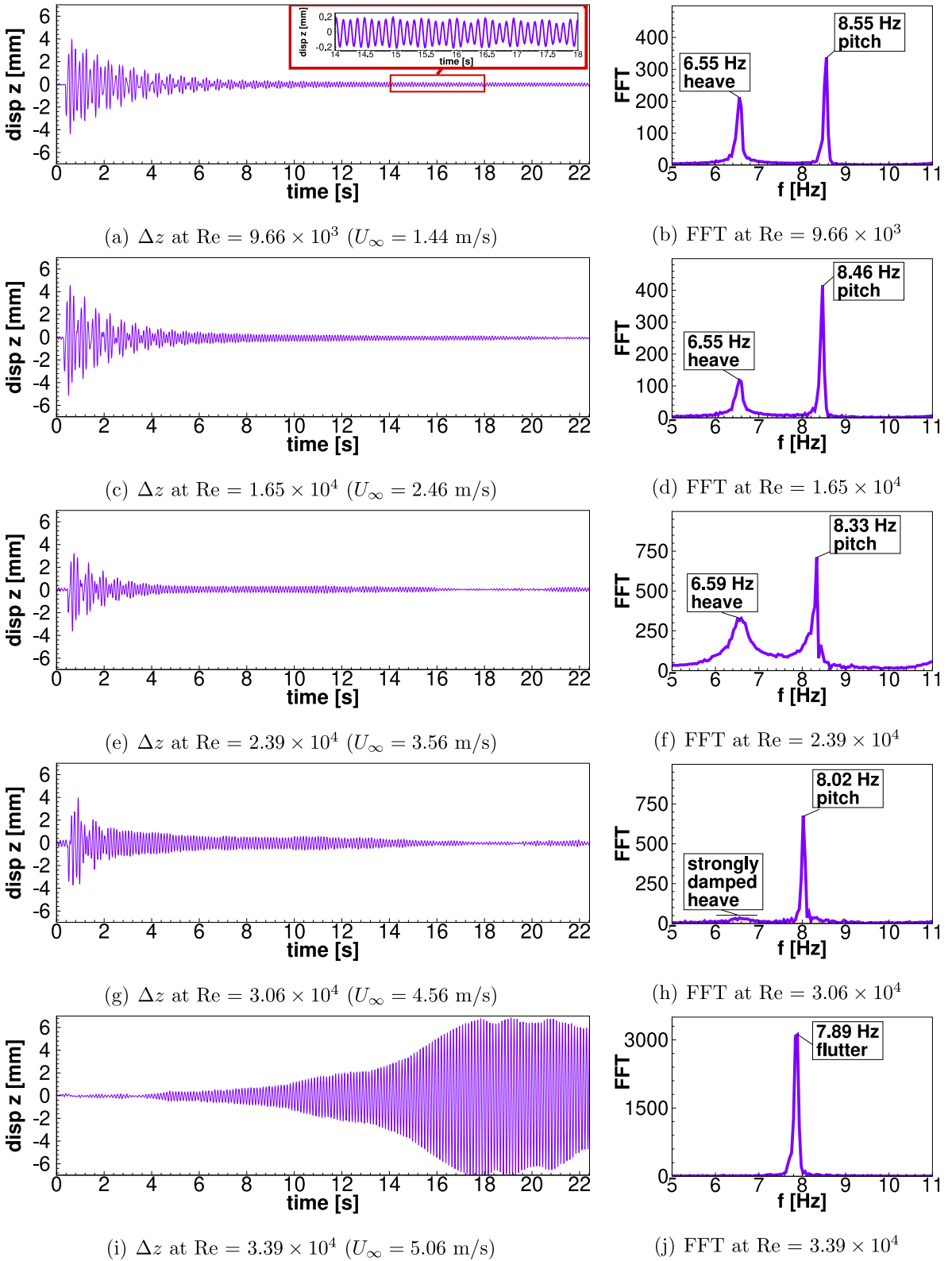


Fig. 16. Case III: DIC measurements at P_w : Time history and frequency response of the motion after a manually introduced disturbance (except for the last case) in the Re range $9.66 \times 10^3 \leq Re \leq 3.39 \times 10^4$ (1.44 m/s $\leq U_\infty \leq 5.06$ m/s).

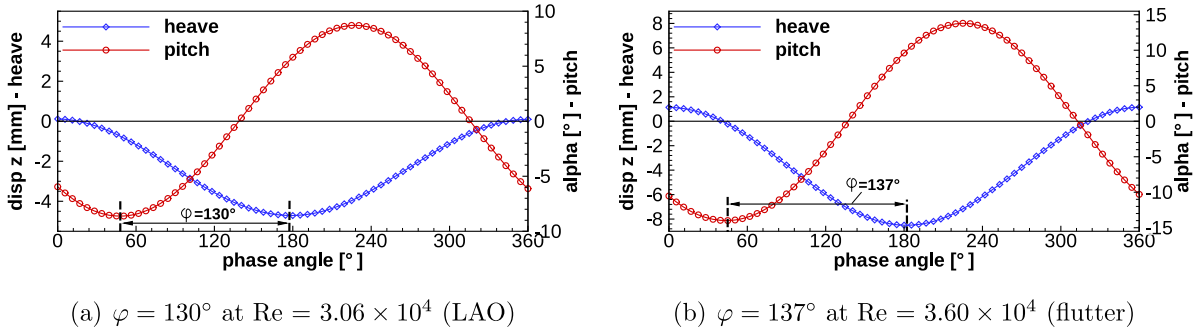


Fig. 17. Case I: Phase-shift angle between pitch and heave associated with large-amplitude oscillations at $Re = 3.06 \times 10^4$ (LAO) and $Re = 3.60 \times 10^4$ (flutter) measured at the two monitoring points P_w and P_h .

an effect on its frequency remaining at 6.55 Hz. Contrarily, the pitch frequency decreased to 8.46 Hz, but its FFT value is slightly increased. This trend continues for $Re = 2.39 \times 10^4$ depicted in Figs. 16(e) and 16(f). Here, the damping of the heave motion is characterized by a broader spectral distribution in the FFT with a frequency of 6.59 Hz measured at the peak value. The pitch frequency has a peak at 8.33 Hz and exhibits increased FFT values. Both frequencies approach each other resulting in a slightly lower beat frequency characterized by $\Delta f = 1.74$ Hz compared to the still-air case ($\Delta f^{2-DOF} = 1.96$ Hz, Table 2). At $Re = 3.06 \times 10^4$ (Figs. 16(g) and 16(h)) the system is still damped by the wind load. Especially the heave motion experiences a very strong damping without any significant peaks in the FFT. Once again, the pitch frequency is decreased to 8.02 Hz at more or less the same peak value of the FFT.

Finally, flutter is observed at $Re = 3.39 \times 10^4$ in Fig. 16(i) at a single characteristic frequency of 7.89 Hz (Fig. 16(j)) which is almost the average value between the heave and the pitch frequency under still-air condition ($f_h^{2-DOF} = 6.55$ Hz and $f_\alpha^{2-DOF} = 8.51$ Hz). In this case no initial excitation is applied to the wing. The increase of the amplitude has an exponential character reaching a peak value after 17 s with a maximum amplitude of $\Delta z = \pm 7$ mm. At about $t = 21$ s the amplitudes are distributed asymmetrical around the zero-line. This behavior is due to a sudden deflection of the torsional springs caused by the applied torque on the fixing screws. These screws are relatively low tightened to withstand a certain rotational moment. When the pitching movement exceeds the maximum angle of the torsional springs ($\alpha = \pm 15^\circ$), the rotational parts run into this limit of the spring construction (see Fig. 4). This procedure is necessary to prevent the damage of the torsional springs. Thus, this case represents flutter, although the amplitudes are (mechanically) restricted beyond 18 s.

6.2. Two-point measurements

6.2.1. Case I: $x_{EG}^I/c \approx 0$

The two-point measurements focus on the two highest Re numbers, where considerable LCO are observed. The data are taken at a fully developed state with nearly constant amplitudes of the LCO with specific emphasis on the LAO phenomenon. First, the LAO behavior at $Re = 3.06 \times 10^4$ depicted in Fig. 17(a) is discussed. In this case the pitch is leading the motion followed by the heave resulting in a phase-shift angle of $\varphi = 130^\circ$. The pitch angle is between $\alpha = \pm 8.5^\circ$, whereas the maximum heave displacements are mainly negative with a maximum found at $\Delta z_h = -4.3$ mm. This yields a heave amplitude in the range of $\Delta \hat{z}_h = \pm 2.6$ mm around its mean deflection ($\Delta \bar{z}_h = -2.12$ mm).

At $Re = 3.60 \times 10^4$ the general characteristic of the motion between pitch and heave is similar to the Re before. However, the phase-shift angle has slightly increased to $\varphi = 137^\circ$. The maximum pitch angle ($\alpha = \pm 14^\circ$) and the maximum heave displacements ($\Delta z_h = -8.1$ mm) are about twice as large as for the lower Re leading to a mean deflection $\Delta \bar{z}_h = -3.8$ mm. The heave amplitude around the mean deflection is in the limits $\Delta \hat{z}_h = \pm 4.7$ mm.

6.2.2. Case II: $x_{EG}^{II}/c \approx -0.022$

Two separate two-point measurements were carried out for the highest Re number (8.77×10^4) in order to get a deeper insight into the LCO characteristics of the airfoil. First, the time span in which SAO are observed is analyzed and presented in Fig. 18.

For this particular case the airfoil was not disturbed by a manual excitation in order to receive the pure SAO phenomenon. A time history is presented here since there is no well developed sinusoidal displacement pattern visible in the signal to which a phase-shift angle would fit. The heave displacements are marginally larger than the pitch displacements and seem to follow more or less an oscillatory motion associated with one main frequency. Contrarily, the pitch motion shows a more irregular behavior. However, both signals contain identical frequencies with somewhat different FFT peaks found at 3.56 Hz, 7.39 Hz and 11.30 Hz.

The lowest frequency observed (3.56 Hz) corresponds to $St = f c \sin(\alpha_{max})/U_\infty = 1.9 \times 10^{-4}$, where St is the Strouhal number based on the maximum angle of attack ($\alpha_{max}^{SAO} \approx 0.4^\circ$) of the airfoil used for definition of the characteristic length

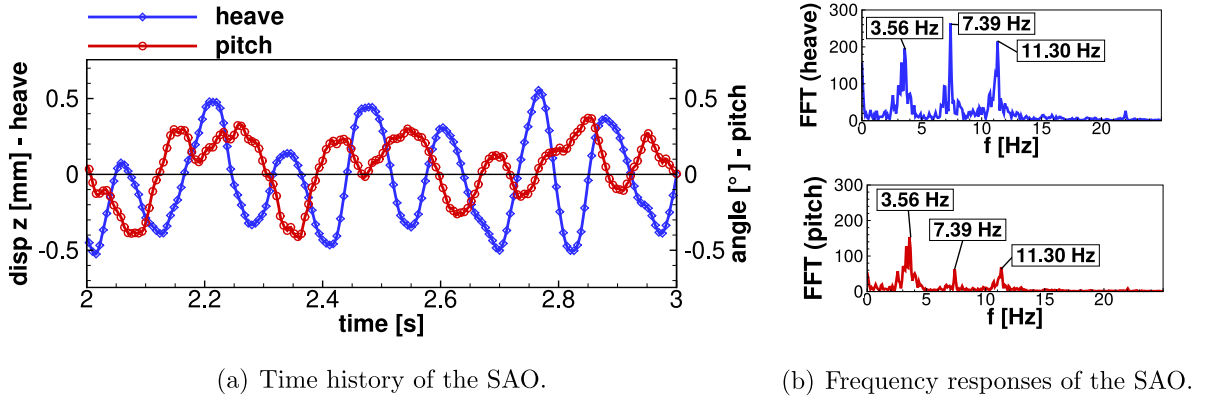


Fig. 18. Case II: Signal of heave and pitch at $Re = 8.77 \times 10^4$ measured at two monitoring points during the SAO.

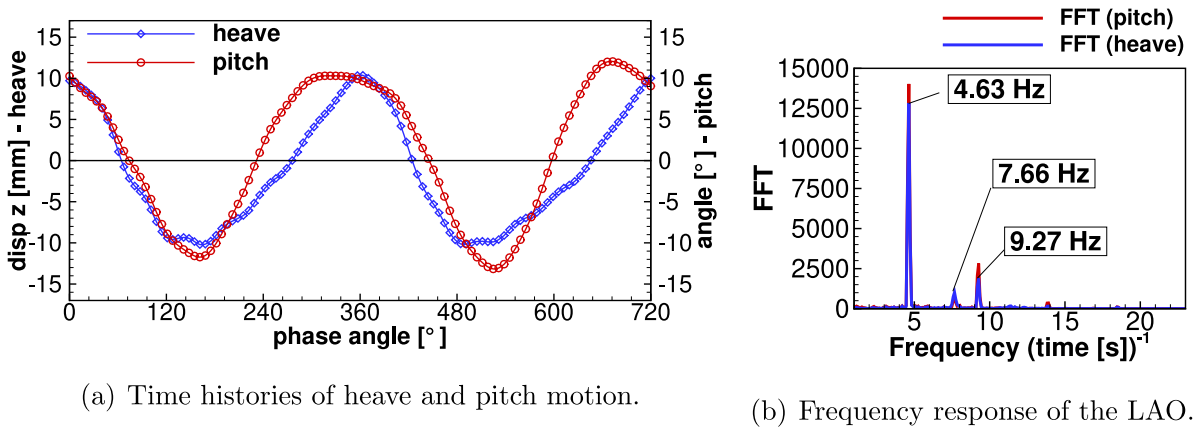


Fig. 19. Case II: LAO characteristics at $Re = 8.77 \times 10^4$: A phase-shift angle between pitch and heave is not clearly defined. The FFT reveals a main frequency at $f = 4.63$ Hz and its first harmonic ($f = 9.27$ Hz).

($c \sin(\alpha_{\max})$). The source of this low frequency is unclear, since all relevant eigenfrequencies of the elastic structure are well above this frequency.

The second frequency (7.39 Hz) was already visible in the single-point measurement (Fig. 15(j)), with a local peak at 7.65 Hz. It corresponds to the pitch frequency of the airfoil observed at lower Re numbers.

The third frequency (11.30 Hz) is related to the third DOF (rolling around the x -axis) which was not filtered out as in the case of the 1-DOF measurements in still air in order to maintain possible higher frequency responses in the signal. As stated in Section 4, the expansions of the speckle pattern are not large enough to clearly identify this motion directly from the DIC data. However, this eigenfrequency is confirmed by analytical predictions.

The second two-point measurement focuses on the LAO at the same Re number. For this case a manual disturbance was brought up in order to receive the desired LAO phenomenon. After the system has settled at a constant amplitude, the measurements were carried out. The results are depicted in Fig. 19.

Fig. 19(a) shows an approximately sinusoidal pattern for the heave and the pitch motion with some irregularities at the maxima. The heave displacements are between $\Delta z_h = \pm 10$ mm and the pitch angle oscillates between $\alpha = \pm 14^\circ$, which is in the range of the stall angle of the NACA 0012. A phase-shift angle between the pitch and heave motion is not clearly determinable, since the sinusoidal pattern is not regular especially at the maxima. Thus, the behavior is opposite to case I.⁵ The corresponding frequency response is given in Fig. 19(b). The most prominent frequency of the LAO is found at $f = 4.63$ Hz ($St = 0.0086$) together with its first harmonic at $f = 9.27$ Hz ($St = 0.0171$) based on $\alpha_{\max}^{LAO} = 14^\circ$. An early study by Jones (1933) reported a similar Strouhal number of about 0.006 for a fixed wing around the maximum lift angle. Jones observed that this low frequency originates from flow oscillations due to thin-airfoil or leading-edge stall.

⁵ Note that for this case an analysis of a systematic error occurring in the present study due to the monitoring point on the heave spring is provided in Appendix. This error is very small on the average and does not affect the discussion of the measurement. Nevertheless, the authors are aware of this error and documented this issue carefully.

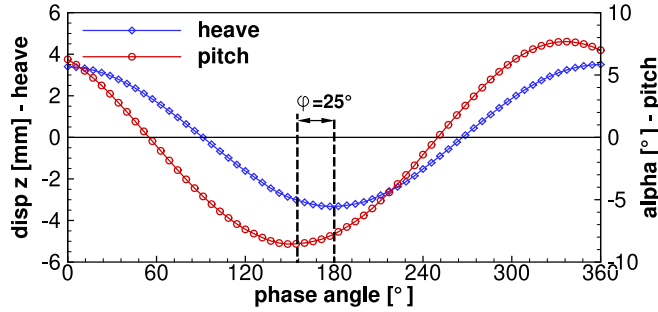


Fig. 20. Case III: Phase-shift angle of $\varphi = 25^\circ$ between pitch and heave at $Re = 3.39 \times 10^4$ measured at two monitoring points.

Bragg et al. (1993, 1996) and Broeren and Bragg (1999) measured low frequency oscillations in the wake of an LNR(1)-1007 airfoil with St numbers around 0.02 in the Re range $4 \times 10^4 \leq Re \leq 1.4 \times 10^5$. It is argued by the authors that this low St number is caused by a cyclic growth and bursting of an LSB on the suction side of the airfoil. This flow characteristic was found at the boarder to stall at large angles of attack. In order to get a deeper insight, Broeren and Bragg (2001) investigated the wake flows of 12 airfoils with different stalling characteristics at $Re = 3 \times 10^5$. All airfoils showed similar spectra in the wake with low frequency flow oscillations around $St = 0.02$ and their higher harmonic at $St = 0.04$. A key role for the low frequency flow oscillation was attributed to the presence of the LSB, which appeared close to stall. When eliminating the LSB these fluctuations were significantly reduced. The issue was supported by the study of Rinoie and Takemura (2004) investigating the behavior of LSBs forming near the leading edge of a NACA 0012 airfoil at $Re = 1.3 \times 10^5$ based on laser-Doppler anemometry measurements. In their study the airfoil was set to $\alpha = 11.5^\circ$. In this configuration a remarkably low frequency of 2 Hz ($St = 0.008$) was measured which was assigned to one oscillation cycle (formation to burst) of the LSB. Based on this discussion it is obvious that the Strouhal number related to the frequency of $f = 4.63$ Hz lies in the range observed for the formation and bursting of LSB. Therefore, it is most likely cause of the frequency detected.

As in case of the SAO, it is assumed that the small frequency peak presently observed at $f = 7.66$ Hz is related to the eigenfrequency of the pitch motion. Note that similar frequencies are detected for the pitch motion in the single-point investigation (see Fig. 15(j)).

6.2.3. Case III: $x_{EG}^{III}/c \approx +0.059$

The two-point measurements of case III concentrate on the flutter motion. As in the cases before, the measurements were carried out in the developing stage after significant amplitudes of the flutter phenomenon were present. The outcome is depicted in Fig. 20.

In this case the heave follows the pitch with a phase-shift angle of $\varphi = 25^\circ$. Hence, in accordance with case I the pitch is leading again but with a significantly smaller phase shift than observed for case I (here $\varphi = 137^\circ$ at flutter). The pitch angle is $\alpha = \pm 8.5^\circ$ and the heave displacements are about $\Delta z_h = \pm 3.4$ mm.

In summary, case I and case III show similar characteristics when flutter appears with the largest difference found in the phase-shift angle between heave and pitch ($\varphi = 137^\circ$ vs. $\varphi = 25^\circ$). The motion of both DOF follows a well-defined sinusoidal pattern with one characteristic frequency in each case. However, for case I the displacements of the heave motion are mainly negative, while case III oscillates symmetrically around $z = 0$ mm. Contrary to the former configurations, case II exhibits an oscillatory behavior closest related to stall flutter with an almost in-phase motion pattern between the heave displacement and the pitch angle. Here, the driving FSI mechanism is attributable to the massive flow separation at the leading edge on the suction side of the airfoil resulting in a sudden redistribution of the pressure. This effect alternates between positive and negative incident angles visible as a strong “flapping” movement.

6.3. Motion patterns from DIC

A major advantage of the 3D-DIC measurements compared to displacement sensors is the three-dimensional data obtained from the speckle area. These data are subsequently used to visualize the motion of the wing including heave and pitch for the most interesting cases already discussed in the former sections based on two-point measurements (P_w and P_h). In the following, two lines are extracted along each speckle area (on the heave spring and the wing) in order to get a deeper insight into the actual dynamic behavior of the airfoil during an arbitrary cycle. The side views presented in Figs. 21 to 23 are focusing on the deformation of the heave spring and the motion of the wing including pure pitch. The color coding of the graphs is as follows: The deformation of the heave spring is illustrated as a blue line. The speckle pattern applied to the heave spring contains DIC data between $22 \text{ mm} \leq l \leq 54 \text{ mm}$ (see Fig. 3, right image). A third-order best-fit polynomial is used to extrapolate along the complete expansion of the spring based on the DIC measurements (blue diamonds) considering a fixed point at $x = 0$ mm and $z = 0$ mm, where the heave spring is mounted to the frame.

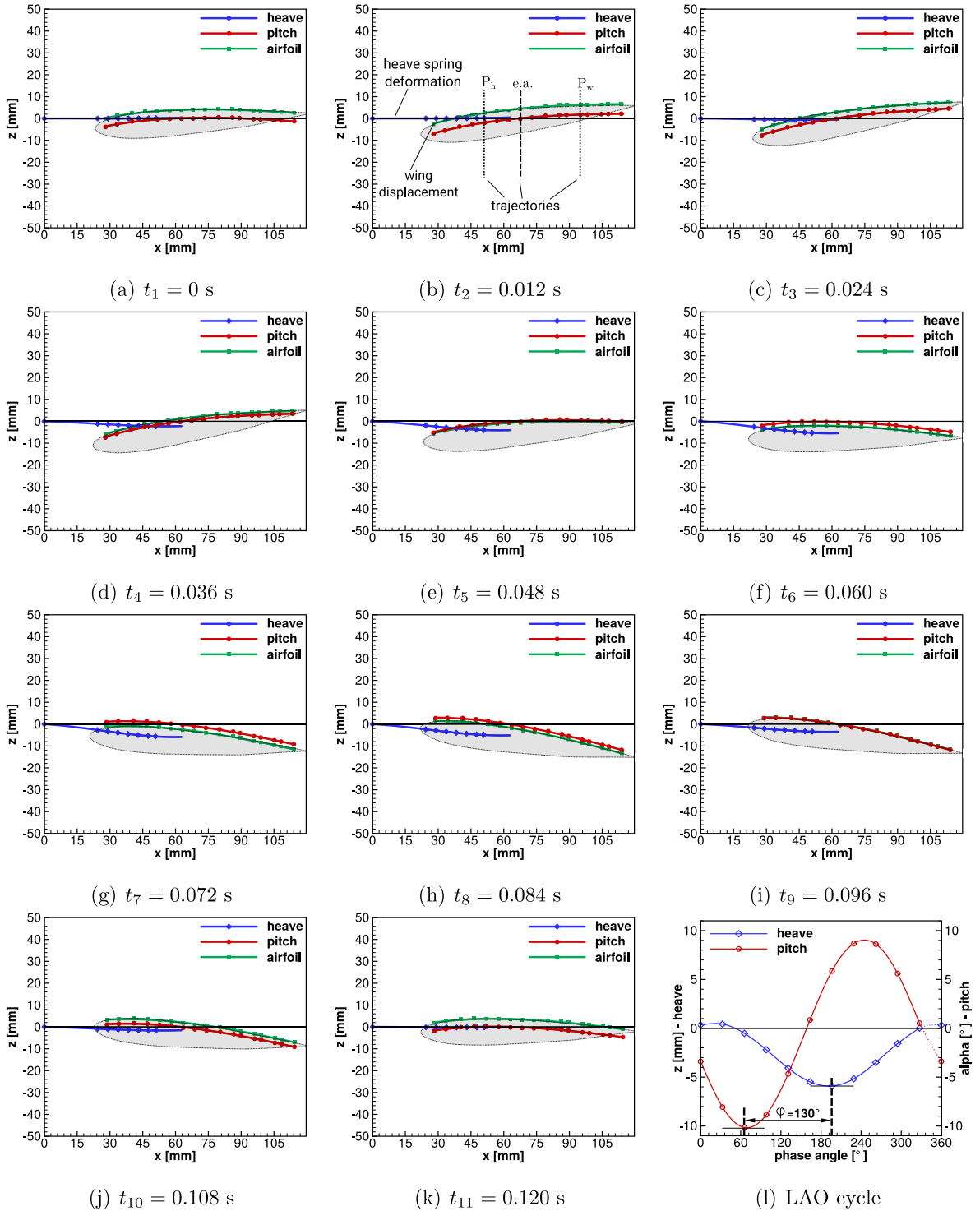


Fig. 21. Case I: Time history of the locations of the heave spring (blue), the pitch (red) and the airfoil (green) within one LAO cycle at $Re = 3.06 \times 10^4$ visualizing the phase shift between the pitch angle and the heave displacements. (For interpretation of the references to color in this figure legend, the reader is referred to the web version of this article.)

The speckle pattern on the wing covers a large part of the upper surface and is illustrated in green and square symbols. Additionally, a NACA 0012 airfoil is sketched into each plot in order to enhance the visualization. Finally, the pure pitch is represented as a red line (circle symbols) predicted from the maximum heave displacement and the actual position of the wing in analogy to the two-point measurements.

6.3.1. Case I: LAO cycle at $Re = 3.06 \times 10^4$

The characteristic LAO cycle of *case I* at $Re = 3.06 \times 10^4$ is presented in Fig. 21. The two-point measurements reveal a phase-shift angle between the heave displacement and the pitch angle of $\varphi = 130^\circ$. This phase shift is also visible in the image series. For this purpose, the vertical position z of the monitoring points P_h and P_w are used (see details in Fig. 21(b)) to extract the data of the heave displacement and the pitch angle. A complete LAO cycle uses the data at each instant in time presented in Fig. 21(l). Note that every symbol in this diagram represents the corresponding snapshot of one image except the last one which is connected to t_{12} closing the period visualized by the dotted line. Following each image, the pitch is clearly ahead of the heave. The maximum downward pitch angle of $\alpha = -10^\circ$ appears at $t_3 = 0.024$ s in Fig. 21(c). The maximum deflection ($z = 5.7$ mm) of the free end of the heave spring is reached significantly later at $t = 0.072$ s depicted in Fig. 21(g) and additionally found in Fig. 21(l). Concerning the heave motion the airfoil oscillates around a negative mean deflection which is due to the reference point, i.e., the fixed point, where the heave spring is mounted to the frame. The pitch angle is nearly symmetrically distributed with a slightly larger maximum negative angle. The large phase-shift angle leads to the interesting dynamic behavior of the airfoil: It reaches its maximum positive pitch angle nearly at the maximum negative deflection of the heave spring. It is assumed that this behavior can be attributed to the coincidence of the c.o.g. and the elastic axis which enables a more or less uncoupled characteristic between rotation and translation. The opposite behavior is discussed for *case III* later. The observed LAO cycle has a period of about 0.13 s corresponding to a frequency of 7.69 Hz slightly deviating from the single-point measurements (7.93 Hz).

6.3.2. Case II: LAO cycle at $Re = 8.77 \times 10^4$

The LAO of *case II* is associated with stall flutter at $Re = 8.77 \times 10^4$. A characteristic LAO cycle is depicted in Fig. 22. In agreement with the two-point measurements the phase shift between pitch and heave is not well defined due to the irregular motion associated with stall flutter. Especially this configuration reveals larger variations between subsequent cycles that lead to slightly altered displacement patterns between different periods. Nevertheless, the image series reveals an almost in-phase motion between heave and pitch best seen in Figs. 22(d) and 22(e), where the heave spring is reaching its minimum ($z = -14$ mm), while at the same time a large negative pitch angle ($\alpha = -14^\circ$) close to the extremum is observed. The dynamic pattern of the LAO in *case II* significantly differs from the other cases, which can be attributed to the position of the extra mass at the leading edge of the airfoil. As discussed for the single-point measurements, this configuration leads to an increased flutter stability since the c.o.g. is shifted in front of the elastic axis. However, when the LAO is triggered at the high Reynolds number of $Re = 8.77 \times 10^4$, the airfoil instantly jumps into the observed stall flutter. Interestingly, the overall movement of the airfoil (green line) gives the impression that the pivot point of the movement is shifted towards the trailing edge. A characteristic pattern is observed during the downward motion in Figs. 22(a) and 22(f). In this case, the heave slightly leads the pitch motion until the maximum vertical deflection of $z = -14$ mm is found at $t_4 = 0.06$ s (Fig. 22(d)). One instant in time later ($t_5 = 0.08$ s) the heave motion is already reversed when the airfoil reaches its maximum negative pitch angle of $\alpha = -17^\circ$ (see Fig. 22(l)) outside the expected limit of the torsional springs. It is assumed that the maximum deformations of the heave springs contribute slightly to the rotation of the airfoil at this velocity. Furthermore, the pitch displacements are marginally overestimated by the chosen measurement approach (see Appendix). This leads to a corrected maximum pitch angle $\alpha_{\max} = -15.39^\circ$ with an maximum error of $\Delta\alpha_{\text{error}}^{\max} = -1.61^\circ$. Based on this estimation and considering a maximum torsional spring rotation angle of $\pm 15^\circ$, the heave spring contributes with -0.39° to the maximum pitch angle. The downward pitch motion is seemingly driven by the increased mass moment of inertia. Afterwards the heave motion pulls the airfoil rapidly upwards (Figs. 22(f) to 22(j)) where the pitch is suddenly overtaking the heave motion (Fig. 22(f)) with a maximum positive pitch angle of $\alpha = +9^\circ$ at $t_9 = 0.16$ s. About one instant in time later ($t_{10} = 0.18$ s) the maximum positive deflection of the heave spring ($z = 8$ mm) is found. The observed LCO has a period of about 0.22 s corresponding to a frequency of 4.54 Hz, which is clearly associated with the major flapping frequency.

6.3.3. Case III: Flutter cycle at $Re = 3.39 \times 10^4$

The oscillation of *case III* is similar to the one of *case I*. However, it is associated with flutter and the respective oscillatory cycle of the airfoil is depicted in Fig. 23 exhibiting a much smaller phase-shift angle of $\varphi = 25^\circ$. In this case the extra mass is applied almost at the trailing edge of the airfoil increasing the mass moment of inertia I_α^E compared to *case I*. The oscillation cycle starts with an upward pitch (Figs. 23(a) to 23(c)) of the airfoil reaching a maximum positive pitch angle of $\alpha = +9.6^\circ$ at $t_3 = 0.024$ s. The maximum upward deflection of the heave ($z = 4.8$ mm) is reached at $t_4 = 0.036$ s. After exceeding this instant in time, the motion of the airfoil is reversed with the negative maximum of the pitch angle of $\alpha = -13.8^\circ$ at about $t_8 = 0.084$ s and the maximum downward deflection of the heave spring of $z = -4.8$ mm at $t_9 = 0.096$ s. In contrast to *case I* the heave spring oscillates symmetrically ($z = \pm 4.8$ mm) around its zero position, whereas the pitch angle reveals larger negative angles. The different phase-shift angle between *case I* and *III* are mainly driven by the difference in the distance x_{EG} between the c.o.g. and the e.a. When increasing or decreasing x_{EG} , the dynamic system reveals a stronger coupling between heave and pitch associated with a smaller phase-shift angle. The investigated oscillation has a period of about 0.128 s corresponding to a frequency of 7.81 Hz, which relates to the flutter frequency found in the single-point measurements (7.89 Hz).

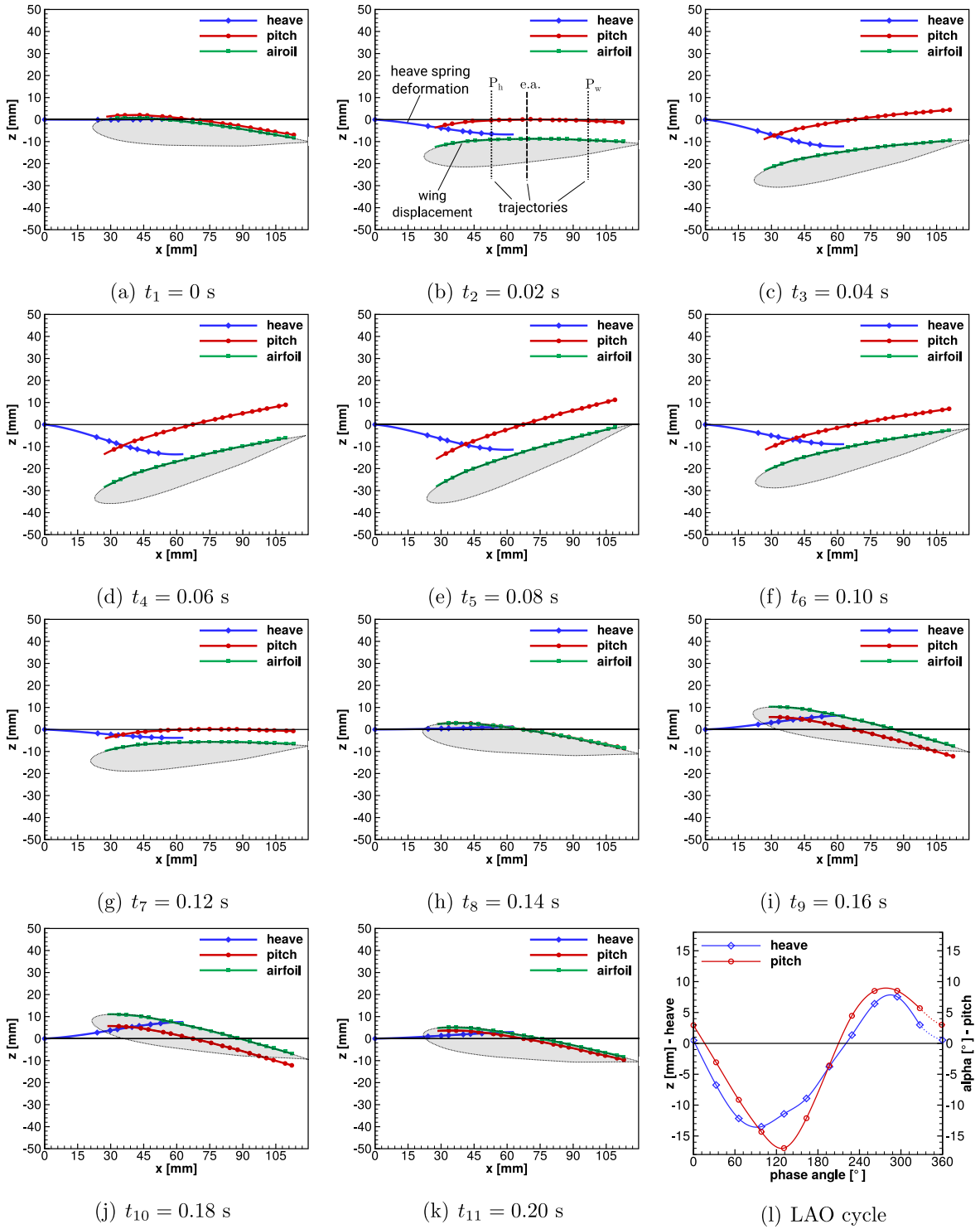


Fig. 22. Case II: Time history of the locations of the heave spring (blue), the pitch (red) and the airfoil (green) within one LAO cycle at $Re = 8.77 \times 10^4$ visualizing the phase shift between the pitch angle and the heave displacements. (For interpretation of the references to color in this figure legend, the reader is referred to the web version of this article.)

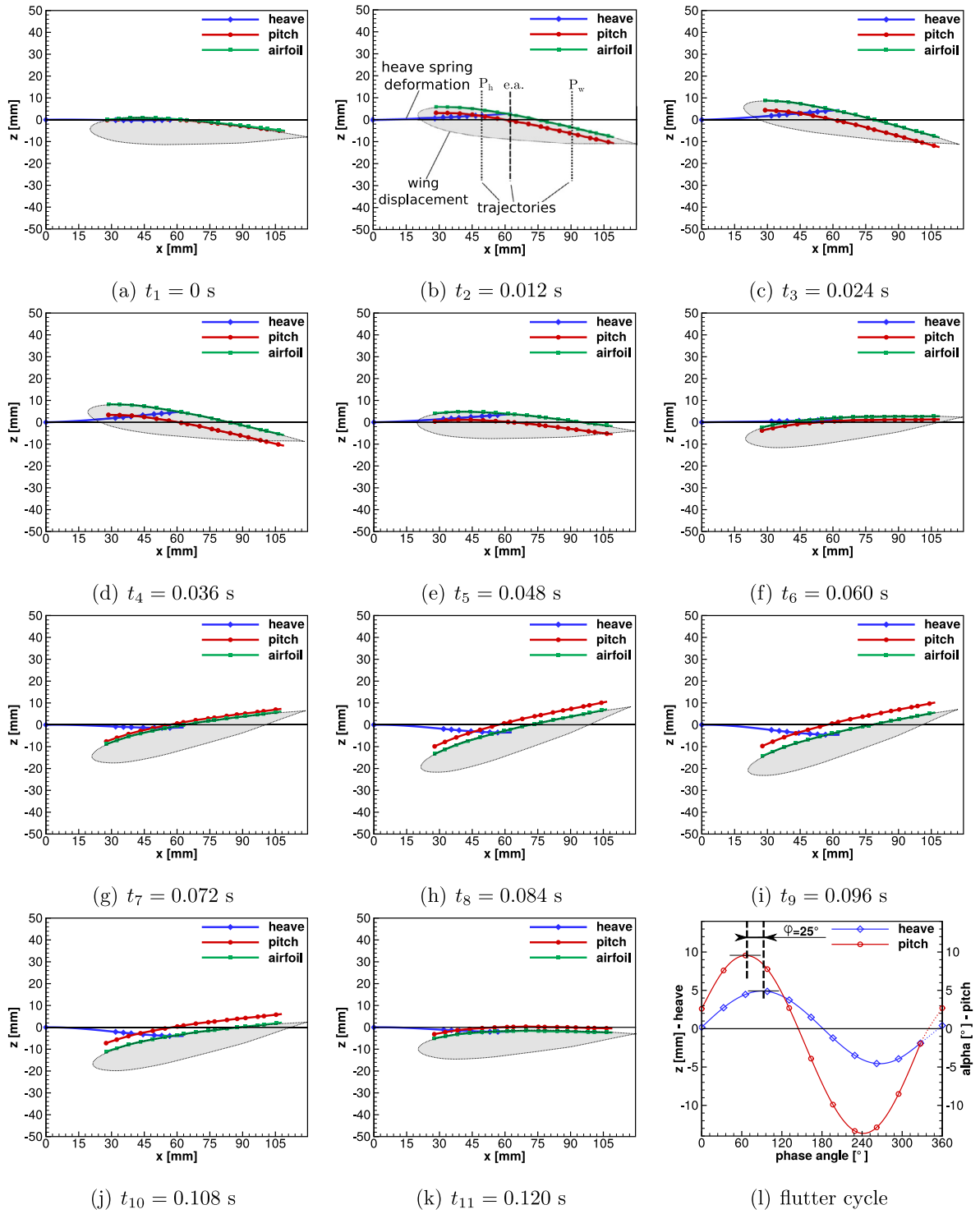


Fig. 23. Case III: Time history of the locations of the heave spring (blue), the pitch (red) and the airfoil (green) within one cycle (flutter) at $Re = 3.39 \times 10^4$ visualizing the phase shift between the pitch angle and the heave displacements. (For interpretation of the references to color in this figure legend, the reader is referred to the web version of this article.)

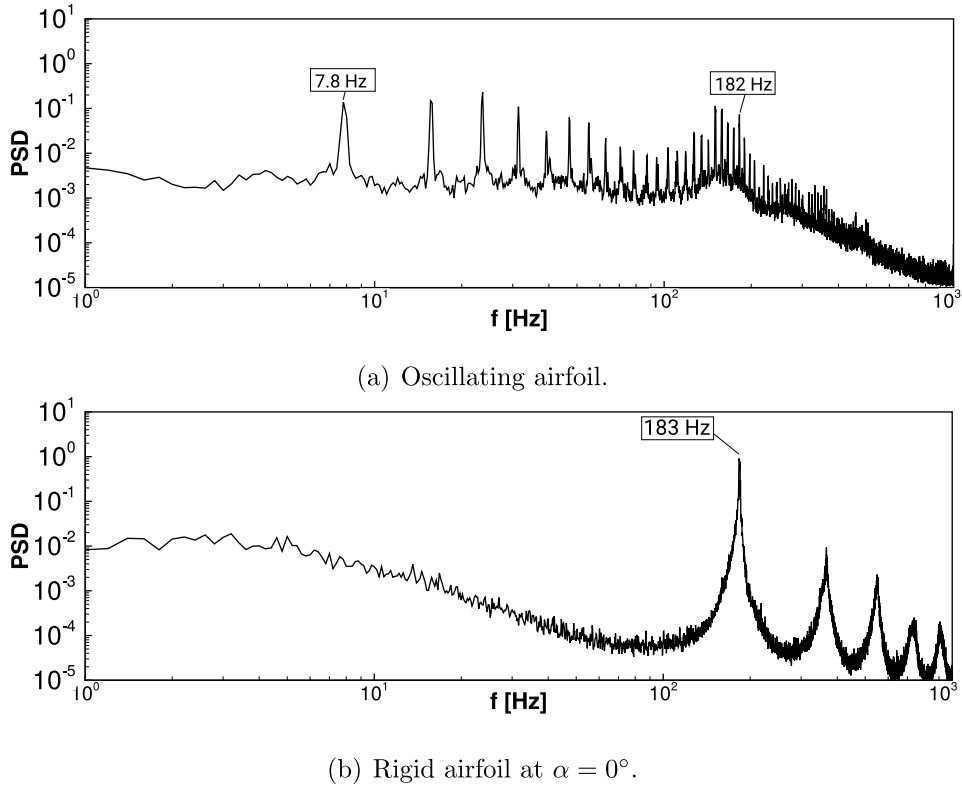


Fig. 24. Case I: Comparison of the power spectral density of the oscillating airfoil with the fully rigid case at $\alpha = 0^\circ$ measured by CTA in the wake at $Re = 3.06 \times 10^4$ (LAO cycle).

6.4. Additional hot-film measurements of the wake flow

In order to get a deeper insight into the excitation mechanisms of each case, additional hot-film measurements (constant-temperature anemometer, CTA) of the flow field in the wake are carried out. The frequency spectra of the CTA measurements (fluid) are compared with the spectra of the DIC measurements (structure). Based on this approach, it is possible to assign certain frequencies of both measurement techniques to the corresponding physical phenomenon. The CTA probe (TSI Type 1201, uni-directional) is located in the wake at a distance of one chord length c behind the wing at the height of the trailing edge with respect to the airfoil at rest with zero angle of attack. Two configurations of the airfoil are considered: First, the wake flow of the oscillating airfoil is measured for each LCO case. Afterwards, the airfoil is set to a fully rigid configuration at $\alpha = 0^\circ$. Taking advantage of both data sets (CTA and DIC), this procedure is used to deduce the FSI mechanism and to attribute the origin of specific frequencies either to the fluid or to the structure.

For each measurement the CTA system (TSI 1750 CTA bridge) is set to a sampling rate of 2000 Hz. A time span of 5 s is recorded containing 10^4 data points. From this sample a power spectral density (PSD) is calculated. This procedure is repeated 100 times to receive an adequate time average of the spectrum based on a total measuring time of 500 s for each measurement.

6.4.1. Case I: LAO and flutter cycle

Fig. 24 depicts the CTA measurements of the LAO of case I, where Fig. 24(a) shows the data of the oscillating wing and Fig. 24(b) presents the spectrum of the rigid wing at $\alpha = 0^\circ$.

The PSD of the oscillating airfoil reveals a dense distribution of clearly defined frequencies across the investigated frequency range of $1 \text{ Hz} \leq f \leq 1000 \text{ Hz}$. The peaks at the fundamental frequency $f_0^1 = 7.8 \text{ Hz}$ and its higher harmonics ($nf_0^1, n = 2, 3, \dots$) are attributed to the LAO motion of the airfoil, which is in very good agreement with the frequency of the DIC data (7.93 Hz). In case of the rigid airfoil a main frequency at 183 Hz corresponding to a Strouhal number of $St = f t_{NACA}/U_\infty = 0.48$ (where $t_{NACA} = 0.12c$ is the thickness of the airfoil used as the characteristic length since $\sin(\alpha) = 0$) is clearly visible in Fig. 24(b) followed by its harmonics. The frequency is attributed to flow instabilities, i.e., the shear layer roll-up appearing in the wake. Similar effects were reported in the experimental investigation of Poirel et al. (2008) ($St = 0.63$ at $Re = 8.01 \times 10^4$) and in the complementary numerical simulations by Métévier et al. (2008) ($St = 0.66$ at $Re = 8.01 \times 10^4$). The distributions of the power spectral densities of both signals (oscillating and rigid airfoil) can be

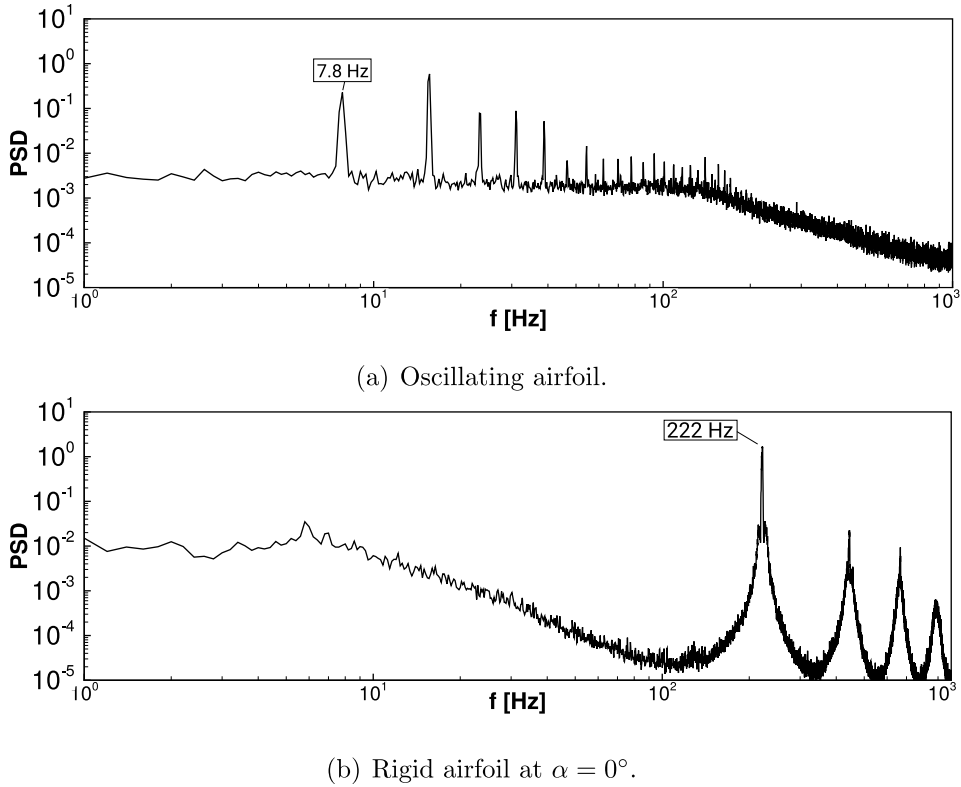


Fig. 25. Case I: Comparison of the power spectral density of the oscillating airfoil with the fully rigid case at $\alpha = 0^\circ$ measured by CTA in the wake at $Re = 3.60 \times 10^4$ (flutter).

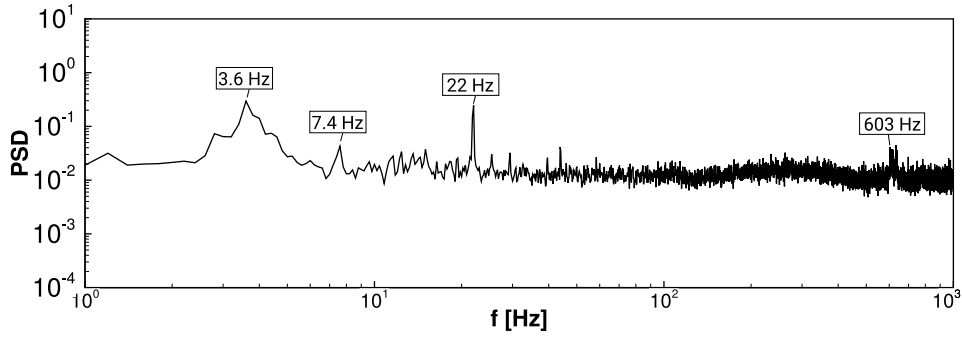
compared in order to assign fluid and structure effects in the spectrum. For example, the PSD of the rigid airfoil solely contains one significant frequency at 183 Hz and its harmonics. The power distribution of the oscillating airfoil is also large in this range ($120 \text{ Hz} \leq f \leq 200 \text{ Hz}$). However, since the CTA probe is fixed in the wind tunnel and does not move with the oscillating airfoil, the peak in the spectrum is not as pronounced as for the rigid case and the effect of the shear layer is hardly visible. On the other hand, all other frequencies can be uniquely assigned to the motion of the structure.

The case of flutter is presented in Fig. 25 showing some remarkable differences from the LAO observed before. First, the rigid airfoil reveals again a dominant frequency at 222 Hz ($St = 0.50$) depicted in Fig. 25(b), i.e., the Strouhal number is nearly constant. The higher frequencies are harmonics of the first peak. Second, this peak completely vanishes for the moving airfoil (Fig. 25(a)) since the airfoil is oscillating and the CTA probe is measuring at a fixed point. Since the amplitude of the oscillation is larger than in the previous case, the effect mentioned above is even stronger with no significant frequency peak found at 222 Hz. All lower frequencies can be attributed to the movement of the airfoil similar to the LAO case. The main frequency of 7.8 Hz coincides with the DIC measurements (7.79 Hz).

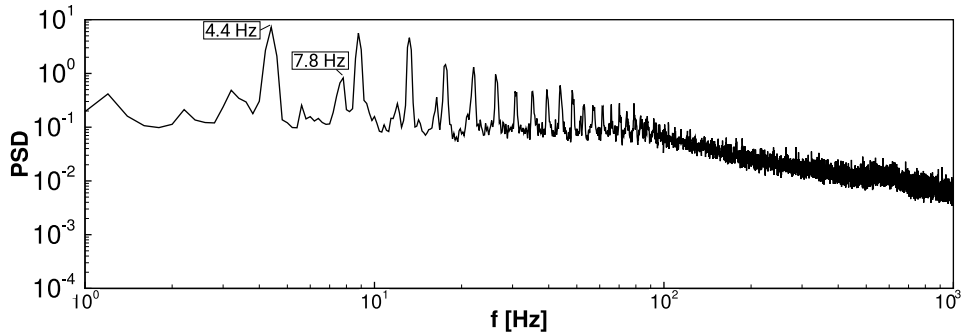
6.4.2. Case II: SAO and LAO cycles

The spectra of the wake regarding the second case are shown in Fig. 26(a) for the SAO, in Fig. 26(b) for the LAO and in Fig. 26(c) for the rigid airfoil at $\alpha = 0^\circ$. The wake flow of the rigid airfoil exhibits a major peak at 598 Hz ($St = 0.54$). With respect to the higher frequency range, the signal of the SAO is similar to the rigid configuration, since the airfoil oscillates moderately. However, the motion of the airfoil is visible in the lower frequency range present at 3.6 Hz and 7.4 Hz. This is similar to the DIC measurements (3.56 Hz and 7.39 Hz). Furthermore, a larger peak is present at 22 Hz. Presently, it is assumed that this frequency originates from the movement of the airfoil, since the rigid case does not contain this frequency. A clarification of the SAO frequencies remains to future work and is further addressed in the numerical counterpart (De Nayer et al., 2020) of this paper. Finally, a higher frequency at 603 Hz ($St = 0.55$) is present, which is related to the separation of the shear layer from the airfoil.

The PSD of the LAO case also contains the dominant flapping frequency of the airfoil (4.4 Hz). Furthermore, a larger peak is found at 7.8 Hz, which is also present in the DIC data (7.66 Hz) and is related to the natural eigenfrequency of the pitch motion.



(a) Oscillating airfoil: SAO cycle.



(b) Oscillating airfoil: LAO cycle.

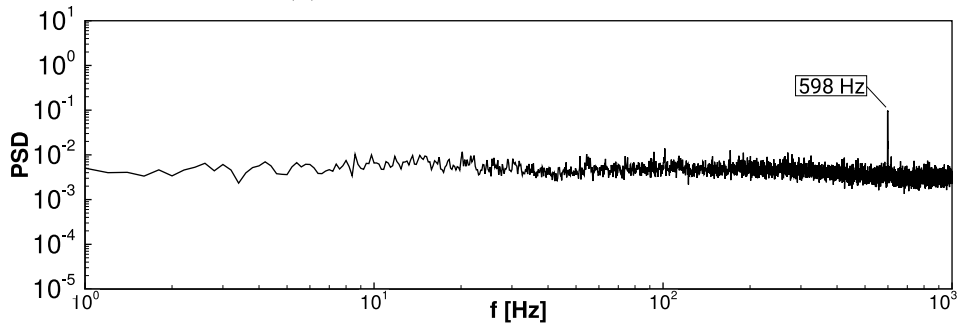
(c) Rigid airfoil at $\alpha = 0^\circ$.

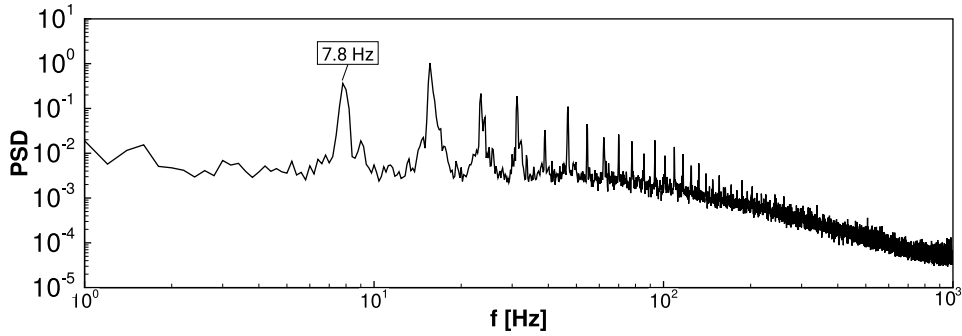
Fig. 26. Case II: Comparison of the power spectral density of the oscillating airfoil with the fully rigid case at $\alpha = 0^\circ$ measured by CTA in the wake at $Re = 8.77 \times 10^4$.

6.4.3. Case III: Flutter cycle

Finally, the spectra of the flutter phenomenon found in *case III* are depicted in Fig. 27. The frequencies originating from the motion of the airfoil visualized in Fig. 27(a) are very similar to *case I*, since the oscillation behavior of the wing is more or less the same except for the phase-shift angle. However, the frequency in the wake of the rigid wing at $\alpha = 0^\circ$ is found at 208 Hz ($St = 0.49$) which is in between the LAO and the flutter scenario of *case I*. Again, the strongly oscillating airfoil has a blurring effect on the high frequency due to the shear-layer instability measured in case of the rigid wing, since the CTA probe is not moving with the airfoil.

7. Conclusions

The dynamic behavior of an elastically mounted NACA 0012 airfoil with 2-DOF (heave and pitch) was investigated in the transitional Re regime ($9.66 \times 10^3 \leq Re \leq 8.77 \times 10^4$). For this purpose, the occurring time-dependent displacements of the airfoil were measured by high-speed three-dimensional digital-image correlation taking three configurations with a variable center of gravity G and a fixed elastic axis E into account. The distance x_{EG} between the c.o.g. and the e.a. alters the



(a) Oscillating airfoil.

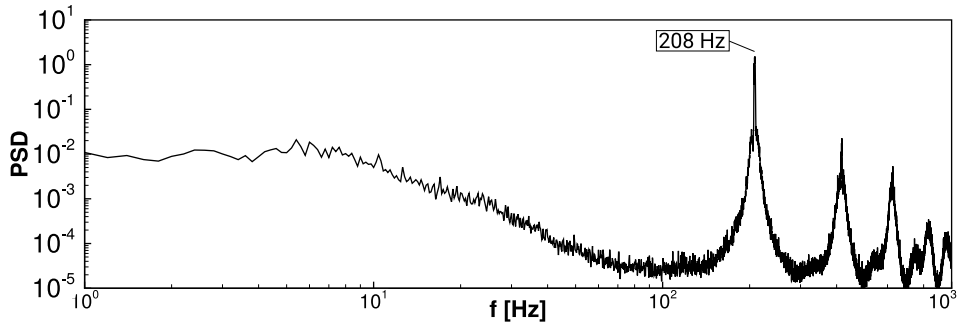
(b) Rigid airfoil set to $\alpha = 0^\circ$.

Fig. 27. Case III: Comparison of the power spectral density of the oscillating airfoil with a fully rigid one set to $\alpha = 0^\circ$ measured by CTA in the wake at $Re = 3.39 \times 10^4$.

dynamic characteristics of the system and is therefore an interesting parameter to study limit-cycle oscillations and flutter. In the present paper, x_{EG} is chosen to coincide with the e.a. (*case I*), shifted in front of the e.a. (*case II*) and behind the e.a. (*case III*). For all three cases the relevant parameters such as the mass, the mass moment of inertia, the spring stiffnesses and the total damping of the setup were determined experimentally by 1-DOF free-oscillation tests in still air. Here, especially the eigenfrequencies of the pure heave and pitch motion were utilized to determine the necessary properties of each configuration. Concerning the damping parameters the current setup without vacuum allows to determine the total damping, i.e., the sum of the material and the fluid damping. Since coupled FSI simulations solely require the material damping, the provided values represent the upper limit for the material damping. However, as demonstrated in De Nayer et al. (2020) the pure material damping coefficients not available from the measurements can be determined based on a series of simulations of 1-DOF free-oscillation tests in still air. The numerical results were compared with the experimental data and the material damping coefficients were systematically reduced until the decay of motion coincides with the measurements.

First, the characteristics of the 2-DOF system in still air were compared with the 1-DOF cases. Especially *case III* (c.o.g. located behind the e.a.) showed a significantly different behavior than the other 1-DOF cases with a higher beat frequency. The main investigation is concerned with the 2-DOF system under increasing wind load considering all three cases. The main findings are:

- In *case I* (c.o.g. \approx e.a.) an increasing damping effect of the motion is observed for a rising free-stream velocity coming along with a convergence of the heave and pitch frequencies. For increasing Reynolds numbers first small-amplitude oscillations followed by large-amplitude oscillations are observed describing a limit-cycle oscillation with a single frequency for pitch and heave. Finally, flutter is found at $Re = 3.6 \times 10^4$. A large phase-shift angle of 130° and 137° is detected for LCO and flutter, respectively, with pitch prior to heave.
- *Case II* (c.o.g. ahead of e.a.) exhibits a completely different behavior. The heave and pitch frequencies do not converge to a single value and the system does not show an instability in the Re range, which was found to be critical for *case I*. Thus, an increased flutter stability is observed as expected. In order to generate LAO, the free-stream velocity has to be nearly doubled. In contrast to the previous case, heave and pitch are almost in-phase leading to stall flutter. No clearly defined phase-shift angle can be determined, since the signals do not possess a sinusoidal shape.
- *Case III* (c.o.g. behind e.a.) is again characterized by a damping effect due to the wind load. However, in contrast to the other cases, the airfoil continues to vibrate with small amplitudes. At a critical Reynolds number slightly lower

than observed for *case I*, flutter sets in. This finding is in agreement with the aeroelastic theory of flutter, which forecasts a lower stability, when the c.o.g. is shifted towards the trailing edge as done in *case III* with respect to *case I*. In accordance with *case I*, pitch is ahead of heave, but with a much smaller phase-shift angle of about 25°.

Additional CTA measurements in the wake of the airfoil carried out for the oscillating as well as the fixed airfoil allowed to assign the different frequencies found uniquely either to the fluid flow or to the motion of the structure.

In conclusion, a variety of challenging test cases for coupled FSI simulations has been identified. Based on the detailed description and the provided characteristic properties of the setups, the different phenomena can be simulated. Since the coupled numerical predictions will provide complete data sets of the structure and the fluid, this pool of information will be used in the subsequent part of this study to get a deeper insight into the relevant physical phenomena.

CRedit authorship contribution statement

J.N. Wood: Conceptualization, Investigation, Methodology, Writing - original draft, Writing - review & editing. **M. Breuer:** Conceptualization, Funding acquisition, Project administration, Methodology, Supervision, Writing - original draft, Writing - review & editing. **G. De Nayer:** Formal analysis, Investigation, Validation, Writing - original draft.

Declaration of competing interest

The authors declare that they have no known competing financial interests or personal relationships that could have appeared to influence the work reported in this paper.

Acknowledgments

The authors want to thank Wolfgang Warnecke (Department of Fluid Mechanics/Helmut-Schmidt University Hamburg) and Benjamin Künzel for the manufacturing, assembly and ongoing improvements on the experimental airfoil flutter setup in the wind tunnel as well as Claudia Thümmel for preliminary studies on the setup.

Appendix. Systematic error of the pitch displacement

The detailed measurements of the limit-cycle oscillations and flutter including two monitoring points are used to separate the heave and pitch motion in order to investigate the occurring displacements and the phase shift between both DOF. Since the monitoring point (P_w) is located on the wing apart from the elastic axis, it contains the information about pitch and heave in a single signal. The second monitoring point P_h is located at the closest measurable point to the elastic axis on the upper heave spring. Both monitoring points are measured simultaneously. Thus, subtracting the pure heave displacement from the wing displacement in the form:

$$\Delta z_\alpha \approx \underbrace{\Delta z_{DIC,w}}_{\text{vertical displacement of } P_w} - \underbrace{\Delta z_{DIC,h}}_{\text{vertical displacement of } P_h} \quad (\text{A.1})$$

leads to an approximation of the pitch displacement. Due to the DIC setup a systematic error arises, when calculating the pitch displacements by Eq. (A.1) depicted in Fig. A.28.

Since the monitoring point on the heave spring is not exactly located on the elastic axis, a small deviation denoted $\Delta z_{h,error}$ ("heave error") between the "true heave" $\Delta z_{h,w}$ of the e.a. and the monitoring point $\Delta z_{DIC,h}$ is present. This systematic error connected to the true heave displacements contributes to a small overestimation of the calculated pitch displacement Δz_α in the following manner:

$$\Delta z_\alpha = \underbrace{\Delta z_{\alpha,w}}_{\text{true rotation}} + \underbrace{\Delta z_{h,w} - \Delta z_{DIC,h}}_{\Delta z_{h,error} > 0} \quad (\text{A.2})$$

The heave error depends on the actual deformation of the heave spring. Obviously, the maximum error is found at the largest upward and downward deformation of the heave spring. In order to approximate the range of $\Delta z_{h,error}$, the LAO of *case II* (see Fig. 19) is used, since this case offers the largest deformations of the heave spring. The error estimation procedure is depicted in Fig. A.29.

For this investigation a line element is taken along the complete speckle area of the heave spring presented by the symbols. The measured deformations of the downward and upward motion of the heave spring are used to extrapolate to the fixed mounting at a distance of 0 mm and the position of the free end of the heave spring (63 mm) by using a third-order polynomial fitting function. The true distance to the elastic axis is found at 69 mm, where its vertical trajectory is shown as a red line. It is assumed that beyond a length of 63 mm no further deformation occurs since the heave spring is tightly fixed to the mounting part used for the coupling between the heave spring and the wing. This is represented by the horizontal blue dashed extension lines at the maximum upward and downward displacements. A close-up view of the actual displacement error is given in the plots on the right. From this approximation the maximum error is estimated for the upward deformation to about $\Delta z_{h,error}^{max,up} \approx 0.35$ mm and for the downward deformation to about $\Delta z_{h,error}^{max,down} \approx 0.75$ mm. Note that the error significantly decreases at positions between the maxima. Based on these estimates, the approach used for the approximation of the pitch displacements Δz_α given by Eq. (A.1) is deemed reasonably accurate.

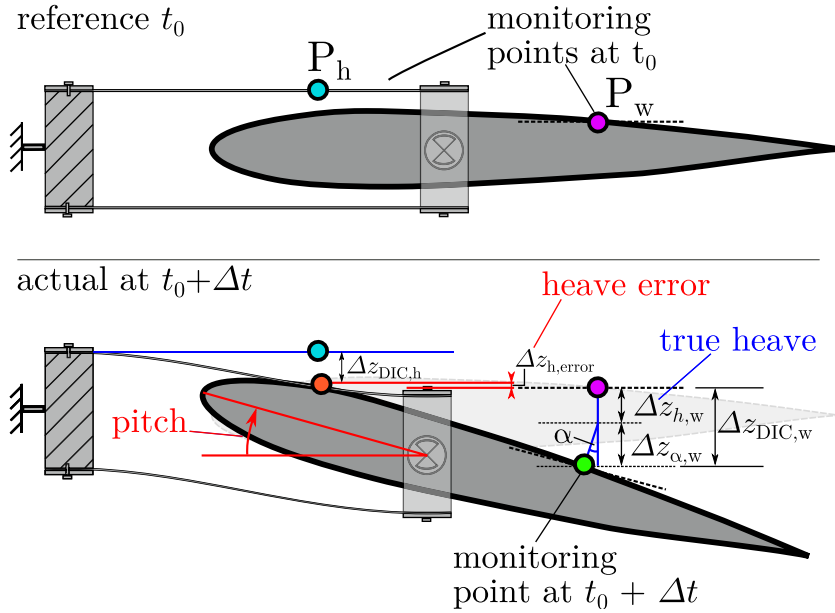


Fig. A.28. Systematic error $\Delta z_{h,error}$ due to the difference between the true vertical displacement $\Delta z_{h,w}$ of the elastic axis and the measured vertical displacement $\Delta z_{DIC,h}$ of the monitoring point P_h on the heave spring. This error contributes to an overestimation of the vertical pitch displacement Δz_α .

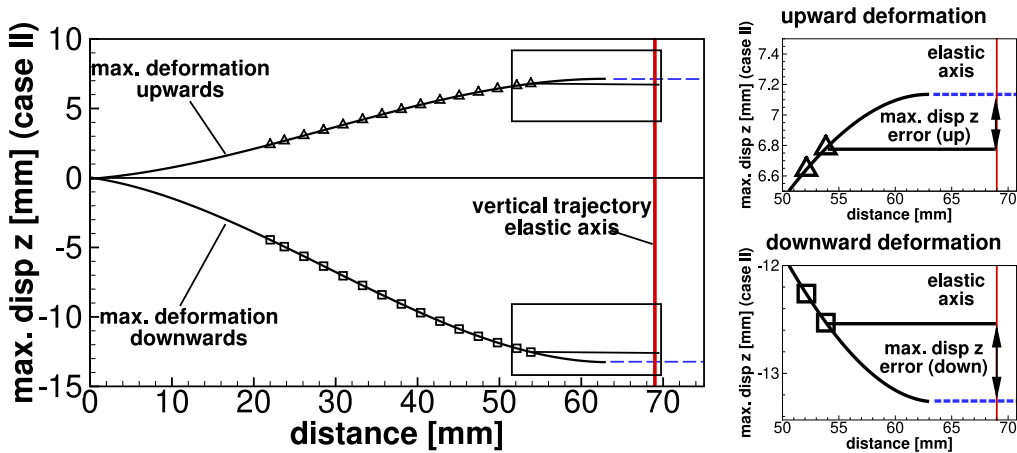


Fig. A.29. Maximum systematic error $\Delta z_{h,error}^{max}$ of the upper and lower vertical displacement associated with the approximation of the pitch displacements Δz_α .

References

Apostolatos, A., De Nayer, G., Bletzinger, K.-U., Breuer, M., Wüchner, R., 2019. Systematic evaluation of the interface description for fluid-structure interaction simulations using the isogeometric mortar-based mapping. *J. Fluids Struct.* 86, 368–399.

Bisplinghoff, R.L., Ashley, H., 2013. *Principles of Aeroelasticity*, second ed. Courier Corporation.

Boudreau, M., Picard-Deland, M., Dumas, G., 2020. A parametric study and optimization of the fully-passive flapping-foil turbine at high Reynolds number. *Renew. Energy* 146, 1958–1975.

Bragg, M.B., Heinrich, D.C., Balow, F.A., Zaman, K.B.M.Q., 1996. Flow oscillation over an airfoil near stall. *AIAA J.* 34 (1), 199–201.

Bragg, M.B., Heinrich, D.C., Khodadoust, A., 1993. Low-frequency flow oscillation over airfoils near stall. *AIAA J.* 31 (7), 1341–1343.

Breuer, M., De Nayer, G., Münsch, M., Gallinger, T., Wüchner, R., 2012. Fluid–structure interaction using a partitioned semi-implicit predictor–corrector coupling scheme for the application of large-eddy simulation. *J. Fluids Struct.* 29, 107–130.

Broeren, A.P., Bragg, M.B., 1999. Flowfield measurements over an airfoil during natural low-frequency oscillations near stall. *AIAA J.* 37 (1), 130–132.

Broeren, A.P., Bragg, M.B., 2001. Unsteady stalling characteristics of thin airfoils at low Reynolds number. In: *Fixed and Flapping Wing Aerodynamics for Micro Air Vehicle Applications*, Vol. 195. *AIAA Progress in Astronautics and Aeronautics*, pp. 191–213.

De Nayer, G., Apostolatos, A., Wood, J.N., Bletzinger, K.-U., Wüchner, R., Breuer, M., 2018. Numerical studies on the instantaneous fluid-structure interaction of an air-inflated flexible membrane in turbulent flow. *J. Fluids Struct.* 82, 577–609.

- De Nayer, G., Breuer, M., 2014. Numerical FSI investigation based on LES: Flow past a cylinder with a flexible splitter plate involving large deformations (FSI-PFS-2a). *Int. J. Heat Fluid Flow* 50, 300–315.
- De Nayer, G., Breuer, M., Wood, J.N., 2020. Numerical investigations on the dynamic behavior of a 2-DOF airfoil in the transitional Re number regime based on fully coupled simulations relying on an eddy-resolving technique. *Int. J. Heat Fluid Flow* in press.
- De Nayer, G., Kalmbach, A., Breuer, M., Sicklinger, S., Wüchner, R., 2014. Flow past a cylinder with a flexible splitter plate: A complementary experimental-numerical investigation and a new FSI test case (FSI-PFS-1a). *Comput. & Fluids* 99, 18–43.
- Dowell, E.H., 2015. *A Modern Course in Aeroelasticity*, fifth ed. Springer Science & Business Media.
- Fung, Y.C., 2008. *An Introduction to the Theory of Aeroelasticity*, third ed. Courier Dover Publications.
- Gomes, J.P., Lienhart, H., 2010. Experimental benchmark: Self-excited fluid-structure interaction test cases. In: Bungartz, H.-J., Mehl, M., Schäfer, M. (Eds.), *Fluid-Structure Interaction II – Modelling, Simulation, Optimization*. In: *Lecture Notes in Computational Science and Engineering*, LNCSE, vol. 73, Springer, Heidelberg, pp. 383–411.
- Gomes, J.P., Lienhart, H., 2013. Fluid-structure interaction-induced oscillation of flexible structures in laminar and turbulent flows. *J. Fluid Mech.* 715, 537–572.
- Gomes, J.P., Münsch, M., Breuer, M., Lienhart, H., 2010. Flow-induced oscillation of a flat plate – A fluid-structure interaction study using experiment and LES. In: Dillmann, A., Heller, G., Klaas, M., Kreplin, H., Nitsche, W., Schröder, W. (Eds.), *New Results in Numerical and Experimental Fluid Mechanics VII*, 16. STAB/DGLR Symposium, Nov. 3–5, 2008, Aachen, Germany. In: *Notes on Numerical Fluid Mechanics and Multidisciplinary Design*, vol. 112, Springer, Heidelberg, pp. 347–354.
- Jones, B.M., 1933. *An Experimental Study of the Stalling of Wings*. Aeronautical Research Committee Reports and Memoranda No. 1588, British ARC.
- Kalmbach, A., Breuer, M., 2013. Experimental PIV/V3V measurements of vortex-induced fluid-structure interaction in turbulent flow – A new benchmark FSI-PFS-2a. *J. Fluids Struct.* 42, 369–387.
- Ke, X.-D., Schreier, H.W., Sutton, M.A., Wang, Y.Q., 2011. Error assessment in stereo-based deformation measurements, Part II: experimental validation of uncertainty and bias estimates. *Exp. Mech.* 51 (4), 423–441.
- Kim, D.-H., Chang, J.-W., 2014. Low-Reynolds-number effect on the aerodynamic characteristics of a pitching NACA 0012 airfoil. *Aerosp. Sci. Technol.* 32 (1), 162–168.
- Kim, D.-H., Chang, J.-W., Kim, H.-B., 2013. Aerodynamic characteristics of a pitching airfoil through pressure-distortion correction in pneumatic tubing. *J. Aircr.* 50 (2), 590–598.
- Lapointe, S., Dumas, G., 2012. Numerical simulations of self-sustained pitch-heave oscillations of a NACA 0012 airfoil. In: *20th Annual Conference of the CFD Society of Canada*, May 9–12, 2012, Canmore, Alberta.
- Métivier, V., Dumas, G., Poirel, D., 2008. Simulations of self-excited pitch oscillations of a NACA 0012 airfoil in the transitional Reynolds number regime. In: *CSME Forum 2008, Canadian Society of Mechanical Engineering*, June 5–8, 2008, University of Ottawa. pp. 5–8.
- Métivier, V., Dumas, G., Poirel, D., 2009. Aeroelastic dynamics of a NACA 0012 airfoil at transitional Reynolds numbers. In: *39th AIAA Fluid Dynamics Conference*, June 22–25, 2009, San Antonio, Texas, AIAA-2009-4034. pp. 1–18.
- Poirel, D., Harris, Y., Benaïssa, A., 2006. Aeroelastic dynamics of a NACA 0012 airfoil in the transitional Reynolds number regime. In: *ASME 2006 Pressure Vessels and Piping/ICPVT-11 Conference*. American Society of Mechanical Engineers, pp. 847–854.
- Poirel, D., Harris, Y., Benaïssa, A., 2008. Self-sustained aeroelastic oscillations of a NACA 0012 airfoil at low-to-moderate Reynolds numbers. *J. Fluids Struct.* 24 (5), 700–719.
- Poirel, D., Mendes, F., 2012. Experimental investigation of small amplitude self-sustained pitch-heave oscillations of a NACA 0012 airfoil at transitional Reynolds numbers. In: *50th AIAA Aerospace Sciences Meeting Including the New Horizons Forum and Aerospace Exposition*. p. 40.
- Poirel, D., Mendes, F., 2014. Experimental small-amplitude self-sustained pitch-heave oscillations at transitional Reynolds numbers. *AIAA J.* 52 (8), 1581–1590.
- Poirel, D., Métivier, V., Dumas, G., 2011. Computational aeroelastic simulations of self-sustained pitch oscillations of a NACA 0012 at transitional Reynolds numbers. *J. Fluids Struct.* 27 (8), 1262–1277.
- Reu, P.L., 2013. A study of the influence of calibration uncertainty on the global uncertainty for digital image correlation using a Monte Carlo approach. *Exp. Mech.* 53 (9), 1661–1680.
- Rinoie, K., Takemura, N., 2004. Oscillating behaviour of laminar separation bubble formed on an aerofoil near stall. *Aeronaut. J.* 108 (1081), 153–163.
- Sicard, J., Sirohi, J., 2013. Measurement of the deformation of an extremely flexible rotor blade using digital image correlation. *Meas. Sci. Technol.* 24 (6), 065203.
- Sirohi, J., Lawson, M.S., 2012. Measurement of helicopter rotor blade deformation using digital image correlation. *Opt. Eng.* 51 (4), 043603.
- Veilleux, J.-C., Dumas, G., 2013. Numerical simulations of experimentally observed high-amplitudes, self-sustained pitch-heave oscillations of a NACA 0012 airfoil. In: *21st Annual Conference of the CFD Society of Canada*, Sherbrooke, Canada, May 6–9, 2013, Paper CFDSC2013-177. pp. 1–12.
- Wood, J.N., 2019. *Experimental Investigations on the Fluid-Structure Interaction of a Deformable and Membranous Hemisphere in Turbulent Flow* (Ph.D. thesis). Professur für Strömungsmechanik, Helmut-Schmidt Universität Hamburg, Germany.
- Wood, J.N., Breuer, M., De Nayer, G., 2018. Experimental studies on the instantaneous fluid-structure interaction of an air-inflated flexible membrane in turbulent flow. *J. Fluids Struct.* 80, 405–440.
- Wright, J.R., Cooper, J.E., 2008. *Introduction to Aircraft Aeroelasticity and Loads*, twentieth ed. John Wiley & Sons.
- Yuan, W., Poirel, D., Wang, B., 2013. Simulations of pitch-heave limit-cycle oscillations at a transitional Reynolds number. *AIAA J.* 51 (7), 1716–1732.
- Yuan, W., Poirel, D., Wang, B., Khalid, M., 2012. Simulations of airfoil limit-cycle oscillations at transitional Reynolds numbers. In: *50th AIAA Aerospace Sciences Meeting Including the New Horizons Forum and Aerospace Exposition*, January 9–12, 2012, Nashville, Tennessee. p. 41.